

Key Points:

- Strong, multipolar magnetic fields may be driven by delamination during top-down solidification of planetesimals
- A Psyche-sized body would solidify in 6–20 Myr and produce a strong magnetic field
- Compositional differentiation leaves solidification time and magnetic field unaltered but results in compositional stratification

Correspondence to:

J. A. Neufeld
j.neufeld@bpi.cam.ac.uk

Citation:

Neufeld, J. A., Bryson, J. F. J., & Nimmo, F. (2019). The top-down solidification of iron asteroids driving dynamo evolution. *Journal of Geophysical Research: Planets*, 124. <https://doi.org/10.1029/2018JE005900>

Received 10 DEC 2018

Accepted 30 MAR 2019

Accepted article online 4 APR 2019

Author Contributions

Conceptualization: Jerome A.

Neufeld, James F. J. Bryson, Francis Nimmo

Writing - Original Draft: Jerome A.

Neufeld, James F. J. Bryson, Francis Nimmo

Writing - review & editing: Jerome A. Neufeld, James F. J. Bryson, Francis Nimmo

The Top-Down Solidification of Iron Asteroids Driving Dynamo Evolution

Jerome A. Neufeld^{1,2,3} , James F. J. Bryson² , and Francis Nimmo⁴ 

¹BP Institute, University of Cambridge, Cambridge, UK, ²Department of Earth Sciences, University of Cambridge, Cambridge, UK, ³Department of Applied Mathematics and Theoretical Physics, University of Cambridge, Cambridge, UK, ⁴Department of Earth and Planetary Sciences, University of California, Santa Cruz, CA, USA

Abstract The cores of some small planetesimals, such as asteroid (16) Psyche, are thought to have been exposed through collisions during the early solar system that removed their mantles. These small bodies likely solidified from the top down representing a fundamentally different solidification regime to that of Earth's core. Here we derive simplified models of the downward solidification of the metallic crust and consider thermal convection and the potential for viscous delamination of the weak, warm base of the crust to provide a buoyancy flux sufficient to drive a dynamo. Thermal buoyancy is very short lived (~1,000 years) and therefore cannot be the source of measured paleomagnetic remanence. In contrast, viscous delamination is found to provide a long-lasting buoyancy flux sufficient to generate an intense, multipolar magnetic field, while not greatly affecting the crustal solidification time. Our results suggest that a Psyche-sized (150-km radius) body solidified in roughly 6.7–20 Myr and that delamination produced a strong magnetic field over much of this time. Finally, including light, insoluble impurities, such as sulfur, results in a partially solid mushy zone at the base of the crust. This further weakens the base of the crust and results in smaller-scale delamination events. Despite a significant change in the dynamics of delamination, the time to total solidification and the predicted properties of the magnetic field are broadly comparable to the sulfur-free case, though we argue this may result in observable compositional stratification of the body.

1. Introduction

Over the last decade, it has become increasingly apparent that some large (≥ 100 -km-scale) asteroids were capable of generating internal core dynamos and magnetic fields early in their history (e.g., Bryson et al., 2015; Carporzen et al., 2011; Fu et al., 2012; Tarduno et al., 2012; Weiss et al., 2008). These are important observations because they place strong constraints on the internal structures and thermal histories of such bodies. For instance, because dynamos are generated within liquid iron cores, any asteroid generating a dynamo must have undergone at least partial internal melting and differentiation. This must be true even if the material recording the magnetic field is itself undifferentiated—presumably because it was close to the surface and did not melt (Elkins-Tanton et al., 2011). Furthermore, the presence of a liquid iron core is not, in itself, sufficient to guarantee a dynamo. In general, heat must be extracted at some minimum rate to drive core convection and dynamo activity (e.g., Nimmo, 2009). Hence, the generation and properties of an asteroid magnetic field may also be used to constrain heat fluxes throughout the body.

Broadly speaking, the thermal evolution of asteroid cores can be divided into three stages (Weiss & Elkins-Tanton, 2013): heating and differentiation, cooling, and solidification.

Heating occurs mainly via the decay of ²⁶Al, which is very energetic but has a half-life of only 0.7 Myr. As long as an asteroid accreted early enough, sufficient energy is released to permit silicate and iron melting and rapid differentiation (e.g., Ghosh & McSween, 1998; Hevey & Sanders, 2006). Early core formation (within a few hundred thousand years of solar system formation) on some asteroids has been confirmed by analysis of the Hf-W isotopic system (Kleine et al., 2009).

Core cooling depends on the ability of the overlying silicates to transfer heat away from the core. Heat transfer is more rapid if the silicates are convecting (Tkalcic et al., 2013) or when heat is transferred by advection of melt (Neumann et al., 2014), rather than simply by conduction. The ability of the near surface to conduct heat will be reduced if a high-porosity regolith is present at the surface of the body (Haack et al., 1990).

On the other hand, some asteroids may have experienced high-energy impacts that removed large parts of their mantles (Asphaug et al., 2006), thereby greatly facilitating subsequent core cooling. The cooling rates of asteroid cores can be constrained from measurements of the size of the exsolution textures that form in iron meteorites upon slow cooling and relatively low temperatures (775 K; e.g., Yang & Goldstein, 2006; Yang et al., 2008, 2010). In particular, very rapid (up to 6600 K/Myr) and variable cooling rates among different members of the same iron meteorite group are most easily reconciled if the parent core lacks an insulating silicate mantle (Yang et al., 2007) thus leaving an entirely metallic asteroid. Cooling rates are thus expected to vary widely from body to body, depending on their impact histories.

Solidification of asteroid cores is complicated for two reasons. First, the location of the initial solidification front is controlled by the relative slopes of the adiabat and the solidus. Both are sensitive to various parameters. As a result, solidification can proceed either from the center outward or from the top down (e.g., Williams, 2009). The fluid dynamics of how solidification proceeds in these two cases may be quite different—see below and Hauck et al. (2006) and Rückriemen et al. (2014), for example. Second, solidification behavior is strongly affected by the bulk sulfur content of the core (e.g., Williams, 2009). Unfortunately, because S is an incompatible element in solid iron, S concentrations in iron meteorites are generally very low, which makes the original bulk S concentration of the core hard to determine (e.g., Chabot, 2004).

However, one important observation is that some meteorite groups display a correlation between metallographic cooling rate (see above) and nickel concentration. Ni is also incompatible (albeit significantly more compatible than S), which means that the Ni concentration in the solid increases as solidification proceeds. The Ni compositions of iron meteorites from the same parent body can therefore be treated as a proxy for the relative order in which the meteorites solidified. As a result, Ni composition-cooling rate correlations can indicate either top-down or bottom-up solidification, depending on the sign of the correlation. In particular, the parent core of the IVA meteorites appears to have crystallized from the top down (Yang et al., 2008), while the IVB body crystallized from the center outward (Yang et al., 2010).

Having examined the stages of asteroid thermal evolution, we now review models of dynamo activity within these small bodies. These models generally fall into two classes: those in which dynamo activity is driven purely by thermal convection and those in which compositional convection (in a variety of forms to be discussed below) is important. Mechanical forcing of asteroid dynamos by either large impacts (Le Bars et al., 2011) or precession (Dwyer et al., 2011) might occur occasionally but is unlikely to be a dominant mechanism in asteroid-sized bodies.

Some theoretical investigations of asteroid dynamo activity have focused on core thermal convection, in which the motion of the core is driven by extraction of heat into the overlying mantle (e.g., Elkins-Tanton et al., 2011; Sterenborg & Crowley, 2013; Weiss et al., 2008). In these studies, dynamo activity ceases once the heat flow out of the core falls below the adiabatic value; this typically occurs within the first few tens of million years, because of the rapid cooling of small bodies.

Once the core starts to solidify, compositional convection can also arise. This mechanism is potentially much more effective at generating a dynamo (Nimmo, 2009), essentially because the density contrasts associated with solidification and light element rejection are typically much larger than those associated with temperature variations. In detail, there are several different modes of compositional convection (Hauck et al., 2006).

The most familiar is the terrestrial case: bottom-up crystallization of a light element depleted iron core, resulting in the release of latent heat and buoyant fluid at the inner core boundary. This mode of crystallization arises due to the pressure dependence of the freezing temperature in larger bodies, has been studied for decades at terrestrial conditions, and has also been applied to small bodies such as the Moon (Laneuville et al., 2014; Scheinberg et al., 2015) and asteroids (Bryson et al., 2015; Nimmo, 2009).

In contrast, for smaller bodies the pressure dependence of the freezing temperature is small so that solidification may proceed from the top of the core, in which case at least two possibilities arise. One possibility is that rapid surface cooling produces small, dense solid particles in the bulk liquid, an “iron snow,” which, being dense, may descend. If this iron snow finds a relatively warm interior, the particles may remelt, releasing relatively dense fluid, which can then descend further, potentially driving a dynamo as it does so (Christensen, 2015; Hauck et al., 2006; Rückriemen et al., 2014; Vilim et al., 2010). More recently Scheinberg et al. (2016) have examined cumulate core solidification, which bears similarities to the iron snow hypothesis. The other

Table 1
Parameter Values Used in This Study

Parameter	Symbol	Value	Unit	Reference
Thermal diffusivity	κ	4.5×10^{-6}	m ² /s	Opeil et al. (2010)
Solid density	ρ_s	7,800	kg/m ³	Bryson et al. (2015)
Liquid density	ρ_l	7,300	kg/m ³	
Density difference	$\Delta\rho$	500	kg/m ³	Laneuville et al. (2014)
Heat capacity	C_p	850	J·kg ⁻¹ ·K ⁻¹	Elkins-Tanton et al. (2011)
Latent heat	L	2.7×10^5	J/kg	Tarduno et al. (2012)
Melting temperature	T_m	~ 1810	K	Ehlers (1972)
Eutectic temperature	T_e	~ 1220	K	Bryson et al. (2015); Tarduno et al. (2012)
Eutectic composition	C_e	~ 32	wt%	Ehlers (1972)
Surface temperature	T_s	200	K	
Coefficient of thermal expansivity	α	10^{-4}	K ⁻¹	Nimmo (2009)
Activation energy	E_μ	3×10^5	J/mol	Sterenberg and Crowley (2013)
Reference viscosity	μ_{s0}	10^{17}	Pa s	Frost and Ashby (1982)
Liquid viscosity	μ_f	10^{-2}	Pa s	Sterenberg and Crowley (2013); Weiss et al. (2010)
Rotational period	p	15,120	s	Hanus et al. (2013)
Magnetic diffusivity	λ_m	1.3	m ² /s	Olson and Christensen (2006)
Solid fraction activation energy	E_ϕ	25		Mei et al. (2002)
Asteroid radius	R	150	km	

possibility is that solidification produces a solid iron crust at the surface of the core that can be unstable to viscous delamination, creating macroscopic dense solid aggregates (e.g., dendrites; Haack & Scott, 1992) which, due to their large size, may not remelt as they descend. This second alternative has been raised as a possibility (e.g., by Scheinberg et al., 2016), but the dynamics, and hence rate, of viscous delamination have not been characterized. In either mechanism of inward solidification, the light fluid expelled during solidification will tend to pool and stagnate near the surface which provides a complicating factor not present in terrestrial bottom-up solidification.

Due to the difficulty in determining the solidification direction in the cores of small bodies from ground-based and satellite measurements, the mechanisms of inward core solidification and magnetic field generation are poorly constrained. However, recent measurements of the IVA iron meteorites provide a well-characterized solidification history of their parent core that could provide key constraints on the nature of inward core solidification. Specifically, this meteorite group displays a wide range of cooling rates that are uncharacteristically quick among iron meteorites (100–6600 K/Myr at ~ 775 K; Yang et al., 2007) and a negative cooling rate-Ni composition trend, all of which indicate that they originate from an inwardly solidifying metallic crust at the surface of an exposed core. Recent paleomagnetic measurements found that the IVA iron meteorites experienced intense (> 100 μT) and directionally varying (timescale of 200 kyr) magnetic fields (Bryson et al., 2017). This solidification and thermal and magnetic history cannot be explained by current theories of inward core solidification: Iron snow is capable of explaining the generation of a magnetic field but does not predict the existence of an inwardly solidifying crust, and the growth of an inactive, stagnant crust explains the cooling rate-Ni composition trend but does not lead to long-lived dynamo generation. Here, we develop a model of a growing crust, the base of which can episodically delaminate and descend, with the resulting stirring generating dynamo activity. Our model is capable of explaining both the inward solidification of the crust and the generation of a magnetic field observed in the IVA meteorites. Furthermore, we predict the properties of the field generated by this mechanism and compare them to the measured field properties to verify our model. Our model is particularly relevant to the solidification of a metallic asteroid such as Psyche with cold surface temperatures and rapid cooling that possibly facilitated rapid crust formation. It is possible that slower-cooling, mantled inwardly solidifying cores (e.g., those in Ganymede and the Moon) may be solidifying through a different mechanism (e.g., iron snow).

Although the solutions we derive are generic, we choose parameters that are specifically applicable to Psyche, which is thought to have similar physical properties, impact history, and thermal evolution to the parent

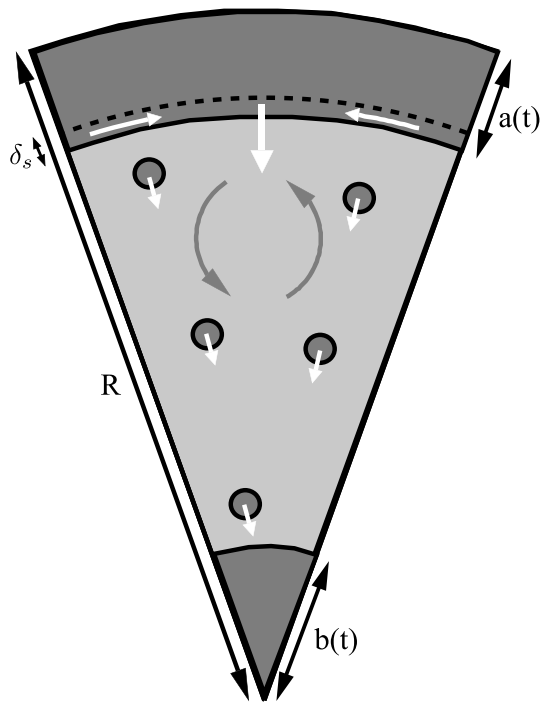


Figure 1. Schematic diagram for a solidifying planetesimal.

core of the IVA iron meteorites. We base our model on the key experimental constraints that this meteorite group originates from an inwardly solidifying metallic crust and that this body generated magnetic fields that were intense and directionally varying. Additionally, we require that shallow depths within this body must have been cold enough ($\lesssim 600$ K) to have recorded a paleomagnetic remanence of this field. The values of the nominal parameters used in our model are summarized in Table 1.

Below we develop a model of the solidification and viscous delamination of a solid iron crust and show how and when the thermal and solid buoyancy fluxes may drive convection in the liquid responsible for observed dynamo activity. In section 2 we consider a warm liquid iron interior, giving rise to the possibility of both thermal and solid buoyancy fluxes. Importantly, we find that the temperature of the interior rapidly approaches the freezing point and that the thermal buoyancy flux can only play a role in driving the planetesimal dynamo for relatively short times. In section 2.4 we consider how the solid buoyancy flux may give rise to a much longer-lasting, yet still vigorous, planetesimal dynamo. In section 3, we show that the inclusion of an incompatible element, for example sulfur, naturally results in the formation of a mushy layer which alters the rheology of the crust and hence the solid buoyancy flux. Finally, we use the results to argue that delamination can drive a planetesimal dynamo and give rise to the strong and directionally varying magnetic fields inferred from paleomagnetic measurements of the IVA meteorites (see below). Throughout we adopt somewhat simplified models capable of analytical solutions. We do so partly because some of the governing

parameters (e.g., solid iron viscosity) are poorly known and partly because analytical solutions provide more insight into the underlying physics.

2. Crustal Growth With Thermal Convection and Solid Delamination

Here we consider an exposed asteroid core that solidifies by the inward crystallization of an iron crust, the base of which can delaminate. We assume, for simplicity, that the large surface radiative heat flux resulting from the absence of a thick silicate mantle leads to the formation of a metallic crust that rapidly becomes mechanically coherent. The radius of the asteroid is R , and its surface is radiatively cooled to a constant temperature below the melting point of pure iron, $T_s < T_m$. This cooling drives the formation and growth of a crust of thickness $a(t)$ (see Figure 1). In the absence of significant concentrations of incompatible elements the temperature at the base of the crust is fixed at the melting point of pure iron, $T_m \approx 1810$ K. Surface cooling may also result in thermally driven convection within the asteroid, and the resulting fluid motion not only acts to mix the fluid interior to an average temperature $\bar{T}(t) > T_m$ but may also produce a significant magnetic field. However, as discussed below, the timescale for magnetic field generation through thermal convection alone is relatively short and therefore unlikely to explain the measured remanent magnetic fields. The formation of a relatively dense (compared to the liquid) crust may also result in delamination and dripping of the crust. We show that the descent of these iron diapirs may also generate sufficient fluid motion to generate a magnetic field and argue that this process of delamination is active over far longer timescales than thermal convection, which are comparable to the timescale for complete asteroid solidification.

The vigorous fluid motion driven by either thermal convection or the mechanical stirring induced by the motion of solid diapirs would present a significant challenge to simulate in detail throughout the full solidification history. Here we instead consider simplified models of both thermal convection and viscous delamination of the iron crust in the framework of classical models of vigorous thermal convection (Howard, 1964) which use a diffusive model of the growth of thermal boundary layers to understand the heat flux from a rapidly convecting interior liquid.

2.1. Diffusive Growth of the Thermal and Viscous Boundary Layers

In the classical conceptual picture of vigorous, high-Ra convection the heat and buoyancy fluxes across an interface may be conceptually modeled by the episodic growth and advection of the thermal boundary.

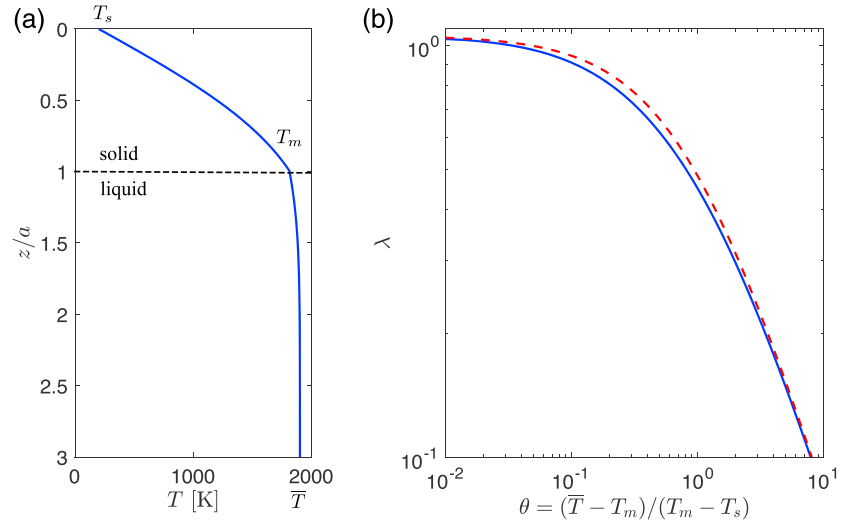


Figure 2. (a) The self-similar profile of temperature with depth through the solid crust and liquid core. (b) The full implicit solution to (7) for λ , which characterizes the solidification rate, is compared against the asymptotic expression (dashed line) provided in (8).

In this picture, the thermal boundary layer grows diffusively to a critical thickness before becoming unstable, at which point it detaches and is advected into the fluid interior on a short timescale compared to the diffusive growth. Models of this process, averaged over many such cycles, provide a quantitative estimate of the heat or buoyancy flux. Here we additionally consider the solidification and growth of the solid iron crust from the hot liquid interior whose temperature is initially above the melting temperature, $T > T_m$. Solidification of a solid into a liquid above its melting point is a classical Stefan problem (Wettlaufer, 2001) and forms the basis for our model of the thermal (liquid) and viscous (solid) boundary layers and hence the buoyancy flux. For simplicity, we treat the specific heat and thermal conductivity of both solid and liquid phases as equal and solve for the diffusion of heat in the crust and thermal boundary layer,

$$\frac{\partial T}{\partial t} = \kappa \frac{\partial^2 T}{\partial z^2}, \quad (1)$$

where z is the depth from the surface and $\kappa = \rho c_p k$ is the thermal diffusivity, written here in terms of the density ρ , specific heat c_p , and thermal conductivity k which for simplicity we take to be equal between phases (and in later sections independent of impurity concentration). For simplicity we adopt a Cartesian description here; while there are analytical solutions for the spherical case (Riley et al., 1974) these are much more complicated, without adding any physical insight. Accordingly, these expressions become increasingly inexact as solidification nears completion. Growth of the boundary layers is driven by the cold surface temperature, T_s , and we additionally require that the solid-liquid interface is in thermodynamic equilibrium, $T = T_m$, and impose conservation of energy at the interface by the Stefan condition,

$$\rho L \frac{\partial a}{\partial t} = k \left. \frac{\partial T}{\partial z} \right|_{a^-} - k \left. \frac{\partial T}{\partial z} \right|_{a^+}, \quad (2)$$

written here in terms of the latent heat L per unit mass. Within the liquid core, the temperature decays to the slowly time-varying, well-mixed temperature of the asteroid interior, $\bar{T}(t)$, well outside the viscous and thermal boundary layers, as illustrated by the solutions in Figure 2a. Hence, the boundary conditions are

$$T = T_s \quad z = 0, \quad (3a)$$

$$T = T_m \quad z = a(t), \quad (3b)$$

$$T \rightarrow \bar{T}(t) \quad z \rightarrow \infty. \quad (3c)$$

There are no obvious, externally imposed length scales since the thermal and solid boundary layers are assumed to be much smaller than the radius of the asteroid, R . Hence, we may expect that the thermal field within the solid crust is a function of the similarity variable

$$\eta = \frac{z}{2\sqrt{\kappa t}}, \quad (4)$$

which can be deduced from a scaling analysis of equation (1), along with a characteristic temperature difference which we take to be that between the melting point and the surface, $\Delta T = T_m - T_s$. Importantly, this immediately also indicates that the crustal thickness is given by

$$a = 2\lambda\sqrt{\kappa t}, \quad (5)$$

where λ is a constant determining the rate of growth.

Solutions to this Stefan problem are well known (see, e.g., Wettlaufer, 2001) and are given in the solid and liquid by

$$T = T_m + (T_m - T_s) \left[\frac{\text{erf}\eta}{\text{erf}\lambda} - 1 \right] \quad 0 < z < a(t), \quad (6a)$$

$$T = T_m + (\bar{T} - T_m) \left[1 - \frac{\text{erfc}\eta}{\text{erfc}\lambda} \right] \quad z > a(t), \quad (6b)$$

respectively (see Figure 2a).

The rate of growth of the solid crust is determined by the Stefan condition and is a function of the Stefan number,

$$S = \frac{L}{c_p \Delta T},$$

which characterizes the relative importance of the release of latent heat to secular cooling. For latent heat $L = 2.7 \times 10^5 \text{ J/kg}$, specific heat $c_p = 850 \text{ J}\cdot\text{kg}^{-1}\cdot\text{K}^{-1}$, and for $T_s = 200 \text{ K}$ and $T_m = 1810 \text{ K}$ (Bryson et al., 2015; Tarduno et al., 2012), and hence $\Delta T = 1610 \text{ K}$, the Stefan number is $S = 0.2$. The Stefan condition therefore reduces to an implicit equation for λ ,

$$S\sqrt{\pi}\lambda e^{\lambda^2} \text{erf}\lambda = 1 - \theta \frac{\text{erf}\lambda}{\text{erfc}\lambda}, \quad (7)$$

as a function of only the Stefan number and the superheat, $\theta = (\bar{T} - T_m)/(T_m - T_s)$, with the full dependence shown in Figure 2b.

When the interior \bar{T} of the asteroid is nearly at the melting point, $\bar{T} \simeq T_m$, this corresponds to $\lambda \simeq \lambda_0 (S = 0.2) = 1.06$, implying that the thermal boundary layer and crust grow at comparable rates. An excellent approximation of the full dependence of λ on the interior temperature is given by

$$\lambda(\bar{T}) = \frac{\sqrt{\pi}}{2\theta + \sqrt{\pi}/\lambda_0}, \quad (8)$$

as shown in Figure 2b, where in general one must find the end point $\lambda_0(S)$ as a function of S by solving equation (7) in the limit $\theta \rightarrow 0$ ($\bar{T} \rightarrow T_m$). This approximation is likely unimportant except in the very early stages of growth where a large superheat may be present ($\bar{T} \gg T_m$), in which case $\lambda \sim \sqrt{\pi}/2\theta$.

We can now assess the stability of the diffusively growing thermal boundary layer and viscous crust, providing both timescales for instability and an estimate of the associated buoyancy flux averaged over many cycles of diffusive growth and instability leading to advection.

2.2. Thermal Boundary Instability and the Thermal Flux

We begin with a review of thermal convection, driven by the temperature difference between the solid-liquid interface and the liquid interior using a boundary layer analysis. In order to calculate the long-term convective fluxes, we adopt the boundary layer argument of Howard (1964) to model the diffusive growth, instability, and advection of the thermal and viscous boundary layers. We focus first on the thermal boundary layer, that is, the low-viscosity liquid region at the top of the convecting, molten interior. Following Howard's original analysis, we note that the thickness of the boundary layer increases diffusively and is of order $\delta_f \sim 2\sqrt{\kappa t}$. This results in a dense thermal boundary layer, and for small variations in the temperature we may use a linear equation of state $\rho = \rho_l[1 - \alpha(T - T_m)]$. A (local) characteristic Rayleigh number for the thermal boundary layer may be defined as

$$Ra_{f,bl} = \frac{\rho_l g(r) \alpha (\bar{T} - T_m) \delta_f^3}{\kappa \mu_f}, \quad (9)$$

based on the time-dependent boundary layer thickness, $\delta_f(t)$, where the fluid density $\rho_l = 7,300 \text{ kg/m}^3$, coefficient of thermal expansion $\alpha = 10^{-4} \text{ K}^{-1}$, liquid viscosity $\mu_f = 10^{-2} \text{ Pa s}$, and thermal diffusivity $\kappa = 4.5 \times 10^{-6} \text{ m}^2/\text{s}$ (Opeil et al., 2010; see Table 1). It is important to note that the boundary layer experiences the local gravitational acceleration,

$$g(r) = \frac{4\pi G}{r^2} \int_0^r \rho(x) x^2 dx \simeq \frac{4}{3} \pi G \rho_0 r \equiv g_0 \frac{r}{R} \quad (10)$$

at radius $r = R - a(t)$, where $G = 6.67 \times 10^{-11} \text{ m}^3 \cdot \text{kg}^{-1} \cdot \text{s}^{-2}$, and we take the fluid density as uniform and equal to ρ_0 . For an asteroid of radius $R = 150 \text{ km}$, the surface gravitational acceleration $g_0 = 0.33 \text{ m/s}^2$, which is the largest gravitational acceleration felt by the growing boundary layer.

In the classical picture of boundary layer growth and instability the boundary layer grows until the local Rayleigh number becomes supercritical, $Ra_{f,bl} \geq Ra_c$, which defines a critical time over which the boundary layer grows before detaching

$$t_f^* = \frac{\delta_f^{*2}}{4\kappa} \simeq \frac{1}{4\kappa} \left(\frac{\kappa \mu_f Ra_c}{\rho_0 g(r) \alpha (\bar{T} - T_m)} \right)^{2/3}. \quad (11)$$

For values representative of a solidifying asteroid, and for critical Rayleigh number $Ra_c \simeq 10^3$ and superheat $\bar{T} - T_m = 10\text{K}$ the timescale for delamination of the thermal boundary layer is very rapid, $t_f^* \sim 37 \text{ s}$.

The thermal instability is therefore rapid and provides an active buoyancy flux into the interior, but only while significant superheat remains ($\bar{T} - T_m$). Modeling the detailed diffusive growth and instability of the thermal boundary layer on such short timescales is an impossibly daunting numerical task. Here, we instead average the diffusive thermal flux from the start of boundary layer growth to instability to approximate the thermal flux into the base of the solid layer above. In detail, the thermal flux may be approximated by the diffusive thermal flux across a boundary layer of thickness δ_f^* ,

$$F_T \simeq k \frac{\bar{T} - T_m}{\delta_f^*}, \quad (12)$$

and hence we find that the thermal flux

$$\begin{aligned} F_T|_{r=R-a} &= k \left(\frac{\rho_0 g \alpha}{\kappa \mu_f} \frac{1}{Ra_c} \right)^{1/3} (\bar{T} - T_m)^{4/3} \\ &= k \frac{\Delta T}{R} \left(1 - \frac{a}{R} \right)^{1/3} \left(\frac{Ra_f}{Ra_c} \right)^{1/3} \theta^{4/3}, \end{aligned} \quad (13)$$

where the gravitational acceleration is evaluated at the base of the crust, $g = g(R - a)$, and where for convenience we recall the definition of the reduced temperature and define a reference fluid Rayleigh number,

$$\theta = \frac{\bar{T} - T_m}{\Delta T}, \quad Ra_f \equiv \frac{\rho_0 g_0 \alpha \Delta T R^3}{\kappa \mu_f}, \quad (14)$$

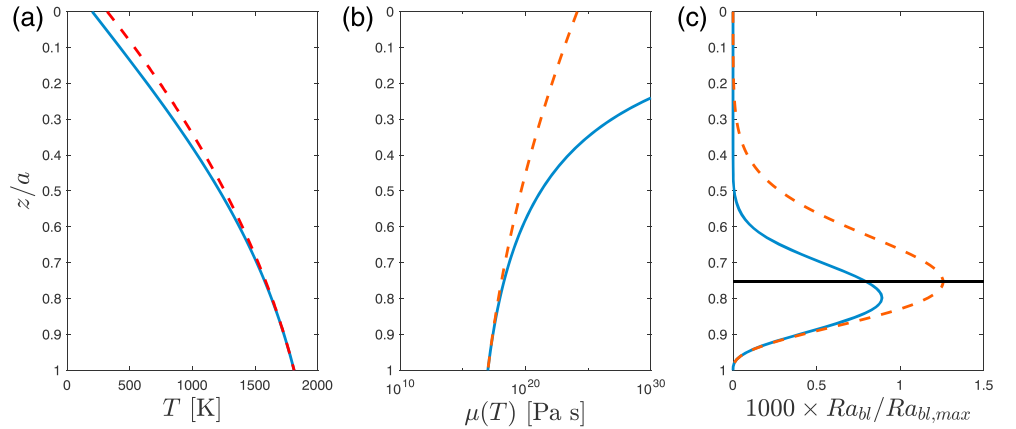


Figure 3. Profiles of (a) the thermal field (equation (6a)), (b) the viscosity $\mu(T(z))$ (equation (17)), and (c) the boundary Rayleigh number, $Ra_{bl}(z)$, (equation (20)) through the crust. The full self-similar solution is given by the solid line, the approximate solution is given by the dashed line (equation (16)), and the (approximate) critical boundary layer depth is given by the solid black line (equation (21)) in panel (c).

respectively. Given the values quoted previously for an asteroid of radius $R = 150$ km, then initially for very thin crust ($a \rightarrow 0$) $Ra_f \simeq 2 \times 10^{23}$. We may already anticipate that the consequence of such vigorous thermal convection, since $Ra_f \gg 1$, is to rapidly drive the temperature of the interior of the asteroid to the melting point, $\bar{T} \rightarrow T_m$, thereby removing the driving for thermal convection.

2.3. Crustal Growth and Viscous Delamination

The growth of the crust is driven by the low surface temperature, $T_s \ll T_m$, and is limited by the release of latent heat on solidification and, to a lesser extent (as we shall see below) the heat flux from the cooling interior for $\bar{T} > T_m$. Anticipating that the initially vigorous thermal convection will rapidly drive $\bar{T} \rightarrow T_m$, we treat the growth of the crust before delamination as a classical Stefan problem. The bottom of the crust is hot and will therefore be unstable to delamination and downwelling if it can flow on a timescale comparable with the rate of solidification. We therefore employ an analysis similar to that considered above for the thermal boundary layer to now model the delamination of the viscous crust. For moderate crustal thicknesses, $a(t)$, the temperature within the crust is given by

$$T \simeq T_m + (T_m - T_s) \left[\frac{\text{erf}(z/2\sqrt{\kappa t})}{\text{erf}(\lambda)} - 1 \right], \quad (15)$$

$$\simeq T_m - 2\lambda^2 S (T_m - T_s) (1 - z/a) [1 + \lambda(1 - z/a)], \quad (16)$$

where z is a coordinate from the surface toward the interior (see Figure 3a for the full and approximate solutions). Taking an Arrhenius viscosity model for the solid iron crust, we may write that

$$\mu_s = \mu_{s0} \exp \left[\frac{E_\mu}{R_g} \left(\frac{1}{T} - \frac{1}{T_m} \right) \right] \simeq \mu_{s0} \exp \left[\frac{E_\mu}{R_g} \frac{T_m - T}{T_m^2} \right], \quad (17)$$

which provides a good approximation to the viscosity near the base of the crust where $T \simeq T_m$. Equivalently, using equation (16), we can write

$$\mu_s \simeq \mu_{s0} e^{\gamma(1-z/a)[1+\lambda(1-z/a)]}, \quad (18)$$

where $\mu_{s0} \simeq 10^{17}$ Pa s (Frost & Ashby, 1982) is the solid viscosity at the melting temperature, $E_\mu = 3 \times 10^5$ J/mol, R_g is the molar gas constant, and the number of e -foldings across the solid crust is given by

$$\gamma = 2\lambda^2 S \frac{E_\mu \Delta T}{R_g T_m^2} \simeq 8.0 \quad (19)$$

for the values in this study.

A consequence of equation (19) is that the viscosity is least viscous at the solid-liquid interface and increases, approximately exponentially, toward the surface so that only a fraction of the boundary layer is unstable

to delamination, the rest being too viscous to convect. A quantitative, and physically motivated, criterion for the thickness of the boundary layer that delaminates can be made by constructing a boundary Rayleigh number,

$$Ra_{bl} = \frac{(a - z)^3 \Delta \rho g}{\kappa \mu(T(z))}, \quad (20)$$

where we note that $g = g(R - a)$. This expression for Ra_{bl} both increases with the thickness of the delaminating layer considered, $(a - z)$, and decreases due to the increasing viscosity with decreasing temperature, $\mu(T(z))$. Profiles of the thermal and hence viscosity structures within the crust are plotted in Figure 3 which also shows that the boundary layer Rayleigh number is sharply peaked near the solid-liquid boundary. Here we assume that the thickness of the delaminating boundary layer corresponds to the depth of the maximal Rayleigh number, $\partial Ra_{bl} / \partial z|_{z_c} = 0$ as indicated in Figure 3c. Physically, the maximum in the boundary Rayleigh number, Ra_{bl} , corresponds to the depth at which viscous dissipation and the potential energy released are equal. For the approximate thermal structure, equation (16), and viscosity structure, equation (18), the critical depth of delamination may be found analytically, so that the thickness of the delaminating layer is

$$\delta_s = a - z_c = a \left(\frac{-1 + \sqrt{1 + 24\lambda/\gamma}}{4\lambda} \right) = \frac{a}{\gamma_e} \simeq 0.24a, \quad (21)$$

for the values in this study (i.e., $\gamma_e \simeq 4$). We note that, to leading order, the thickness of the delaminating boundary layer derived in this fashion is always comparable to the e -folding length of the viscosity scale, $\delta_s = a/\gamma_e \sim a/\gamma$, here modified by the curvature of the thermal profile near the solid-liquid interface. Ultimately, this suggests that only a small fraction of the crust ($\sim 24\%$) is unstable to viscous convection.

A complementary and analogous view of the viscous instability of the crust is as a Rayleigh-Taylor instability of a dense viscous layer (the mobile solid iron crust) overlying a relatively light inviscid layer (the liquid iron core), or equivalently as the convective instability of a fluid with highly temperature-dependent viscosity. Following Molnar et al. (1998), who examined the case of an exponentially varying Newtonian viscosity structure, the minimum timescale for the onset of the Rayleigh-Taylor instability is given by

$$\tau_{RT} \approx 7 \frac{\mu_{s0}}{\Delta \rho g \delta_s}, \quad (22)$$

where the numerical prefactor is based on the maximum calculated dimensionless growth rate of 0.28.

Our previous analysis of the growth by solidification of the iron crust gives the crustal thickness a , and hence, using equations (5), (8), and (21), the timescale for solidification of the weak lower crust is

$$\tau_s = \frac{a^2}{4\lambda^2 \kappa} - \frac{(a - \delta_s)^2}{4\lambda^2 \kappa} \simeq \frac{a \delta_s}{2\lambda^2 \kappa} = \frac{\delta_s^2 \gamma_e}{2\lambda^2 \kappa}. \quad (23)$$

This result highlights that it is the thermal gradient in the crust which drives regrowth of the weak lower layer, so that for a thinner low-viscosity layer the growth timescale is longer (τ_s increases with increasing γ).

The Rayleigh-Taylor instability becomes significant once $\tau_{RT} < \tau_s$, so setting the two timescales equal up to an $\mathcal{O}(1)$ numerical prefactor, $K_T = \tau_s / \tau_{RT}$, we can derive an expression for the critical boundary layer Rayleigh number at which the crust delaminates,

$$Ra_{s,bl} = \frac{g(R - a) \Delta \rho \delta_s^3}{\kappa \mu_{s0}} = \frac{14\lambda^2}{\gamma_e K_T}, \quad (24)$$

and hence an expression for the critical thickness of the crustal boundary layer, δ_s^* , where $Ra_{s,bl} > Ra_c = 14\lambda^2 K_T / \gamma_e$. The timescale for onset of the viscous instability is therefore

$$t_s^* = \frac{\gamma_e \delta_s^{*2}}{2\lambda^2 \kappa} \simeq \frac{\gamma_e}{2\lambda^2 \kappa} \left(\frac{14\lambda^2 K_T}{\gamma_e} \frac{\mu_{s0} \kappa}{\Delta \rho g(r)} \right)^{2/3}, \quad (25)$$

where $\Delta \rho = \rho_s - \rho \approx 500 \text{ kg/m}^3$ is the density difference between solid crust and liquid iron, and in general $\lambda = \lambda(\theta)$ depends on the degree of superheat within the asteroid interior. For reasonable estimates of the physical constants given above (and for $K_T \simeq 0.4$ as discussed below) $t_s^* \sim 33 \text{ kyr}$, which, while much longer

than the timescale for thermal instability, is still much less than the anticipated timescale for solidification of the asteroid. Taking the growth model (equation (5)) for the initial growth of the crust, and recalling that the boundary layer thickness $\delta(t) = a(t)/\gamma_e$, this implies that for the first ~ 68 kyr of solidification the crust is too thin to delaminate and that thereafter the weak lower crust of characteristic thickness $\delta_s^* \simeq 1.6$ km delaminates episodically. We consider that the delamination of this weak, thin boundary layer, for which $\delta_s^* \ll R$, occurs episodically around the crust, the net effect of which is to produce an effective buoyancy flux when considered on timescales longer than t_s^* .

In an analogous manner to the treatment of the thermal flux, we average the repeated growth and delamination of the viscous crust, on timescales much longer than t_s^* , to produce a model for the solid flux,

$$F_s = \Delta\rho \frac{\delta_s^*}{t_s^*}. \quad (26)$$

Hence, using equations (21) and (25), we find that

$$F_s|_{r=R-a} = 2\kappa\Delta\rho \left(\frac{\lambda^4}{14K_T\gamma_e^2} \right)^{1/3} \left(\frac{\Delta\rho g(r)}{\mu_{s0}\kappa} \right)^{1/3}, \quad (27)$$

$$= \frac{\kappa\Delta\rho}{R} \left(\frac{2\lambda^2}{\gamma_e} \right)^{2/3} \left(1 - \frac{a}{R} \right)^{1/3} \left(\frac{Ra_s}{7K_T} \right)^{1/3}, \quad (28)$$

where for convenience we define

$$Ra_s \equiv \frac{\Delta\rho g_0 R^3}{\kappa\mu_{s0}}. \quad (29)$$

Equation (28) shows that the flux increases with the (solid) Rayleigh number, as expected. It also increases with higher diffusivity (because the crust grows more rapidly), and decreases with larger γ_e , because less mass is advected when a thinner layer delaminates. Given representative values for an iron asteroid (Table 1) we find $Ra_s \simeq 1.2 \times 10^6$.

The related case of the convective flux from convection in a fluid with a highly temperature-dependent rheology has been studied previously in a suite of careful laboratory experiments using Golden Syrup (Davaille & Jaupart, 1993). They found that a stagnant thermal boundary layer developed along the cooled upper surface and that the thermal flux due to convection scales with an “effective viscous temperature scale” set by the variation of viscosity at the base of the stagnant region,

$$F_{DC} = Ak \left(\frac{\alpha g}{\mu_{s0}\kappa} \right)^{1/3} \left[-\frac{\mu(T_m)}{(d\mu/dT)_{T_m}} \right]^{4/3}, \quad (30)$$

where the term in square brackets is equivalent to $\Delta T/\gamma$, and report an experimental value of $A = 0.47 \pm 0.03$. Importantly, this dependence on $\Delta T/\gamma$ confirms the dependence on the rheological parameter γ in our expression for the solid flux (equation (28)). This experimental relationship (equation (30)) also provides a value of the prefactor, the magnitude of which provides an experimental estimate for the ratio of solidification to delamination timescales, $K_T = \tau_s/\tau_{RT} \simeq 0.4$. In the classical theory of high Rayleigh number, isoviscous convection (Howard, 1964) this prefactor is small, $K_T \ll 1$, which suggests that the delamination timescale is negligible compared to the timescale of boundary layer growth. In the present context, such a limit would imply that negligible solidification would occur during delamination. As a result, a steady state balance would soon be reached over a cycle of crustal growth and delamination between solidification of the crust and viscous delamination leading to no net crustal growth. Such a balance between growth and delamination would set in rapidly after the first delamination events, leading to a thin, steady state crust whose thickness was of order δ_s^* . This process would continue until the growth of the core through consolidation of these aggregates extended out to the thin crust. Such a thin crust would be unlikely to retain a measurable paleomagnetic signature and so is unlikely given the observational constraints in this context. In contrast, when the prefactor is $\mathcal{O}(1)$ (as is the case here) the timescales of growth through solidification and delamination are comparable, a result which implies that significant solidification and crustal growth can occur even as delamination proceeds. We therefore proceed to use an argument of energy conservation, averaged over the cycle of growth through solidification and delamination, to model the long-term growth of the crust, as described in the following section.

2.3.1. Growth of the Crust and Inner Core and the Evolution of Thermal and Viscous Buoyancy Fluxes

The models developed above, of the thermal and delamination fluxes from the crust to the interior of the asteroid, can be readily used to model the large-scale, top-down solidification of the planetesimal and the possibility of their generating an observable magnetic field. The growth of the crust is driven by cooling from the surface and is limited by the release of latent heat on solidification, the heat flux from the superheated planetesimal interior associated with thermal convection, the specific heat required to cool the thermal boundary layer, and the specific heat required to cool the viscous base of the crust between delamination episodes. Energy conservation, averaged over many thermal and delamination cycles, can therefore be written as

$$\left[\rho L + \rho c_p (\bar{T} - T_m) \right] \frac{\partial a}{\partial t} = k \left. \frac{\partial T}{\partial z} \right|_a - F_T - c_p \left(\frac{T_m - T_c}{2} \right) F_s, \quad (31)$$

where $T_c \simeq T_m - (\partial T / \partial z)_a \delta_s$ is the temperature at the boundary between the mobile and stagnant crust. The terms in equation (31) correspond (from left to right) to the latent heat of solidification, the specific heat associated with cooling the thermal boundary layer from \bar{T} to T_m , heat conduction through the lid, the thermal flux from the liquid interior to the crust associated with vigorous convection, and the average specific heat lost from the boundary during viscous delamination of the solid crust, respectively.

The model of planetesimal solidification is completed by statements of solid mass conservation and of global heat conservation in the liquid. Viscous delamination creates solid aggregates of characteristic size δ_s which therefore sink rapidly toward the center of the planetesimal, creating a cold, inert core. For aggregates of characteristic size $\delta_s(t_s^*) \simeq 1.6$ km, given by equations (21) and (25), the thermal equilibration time is much greater than the transit time from crust to core,

$$\frac{\delta_s^2}{\kappa} \gg \frac{R}{c_D (\Delta \rho g \delta_s / \rho_f)^{1/2}} \quad (32)$$

for drag coefficient $c_D \sim 1$, and hence advection of cold aggregates contributes little to the cooling of the iron liquid in the interior during their descent. As a result, a statement of global conservation of heat within the liquid core can be written as

$$\rho c_p \frac{4}{3} \pi \left[(R - a)^3 - b^3 \right] \frac{\partial \bar{T}}{\partial t} = -4\pi (R - a)^2 F_T, \quad (33)$$

where $b(t)$ is the radius of the stagnant, cold core. The reduction of superheat in the liquid iron core is entirely through the convective heat flux toward the iron crust. Likewise, conservation of solid mass constrains the radius of the core, $b(t)$, and is given by

$$\rho_s 4\pi b^2 \frac{\partial b}{\partial t} = 4\pi (R - a)^2 F_s. \quad (34)$$

Growth of the inner core is driven solely by the solid flux produced by viscous delamination from the base of the solid iron crust.

Equations (31), (33), and (34) specify completely the evolution of the asteroid. Here we further simplify the analysis by approximating $\partial T / \partial z|_a \simeq 2\lambda^2 S (T_m - T_s) / a$, in keeping with equation (6a), and by writing the equations for asteroid evolution in terms of two nondimensional parameters

$$\begin{aligned} F_T &\equiv \left(\frac{Ra_f}{Ra_c} \right)^{1/3} \simeq 2.3 \times 10^7, \\ F_s &\equiv \frac{\Delta \rho}{\rho} \left(\frac{2\lambda^2}{\gamma_e} \right)^{2/3} \left(\frac{Ra_s}{7K_T} \right)^{1/3} \simeq 3.31, \end{aligned} \quad (35a,b)$$

characterizing the thermal and solid fluxes, respectively. The equations for conservation of energy at the solid-liquid interface and for the evolution of the temperature of the liquid interior and the radius of the core are therefore

$$(S + \theta) \frac{\partial a}{\partial t} = 2\lambda^2 S \frac{\kappa}{a} - \frac{\kappa}{R} F_T (1 - a/R)^{1/3} \theta^{4/3} - 2\lambda^2 S \frac{\kappa}{R} (1 - a/R)^{1/3} \frac{F_s}{2\gamma_e}, \quad (36)$$

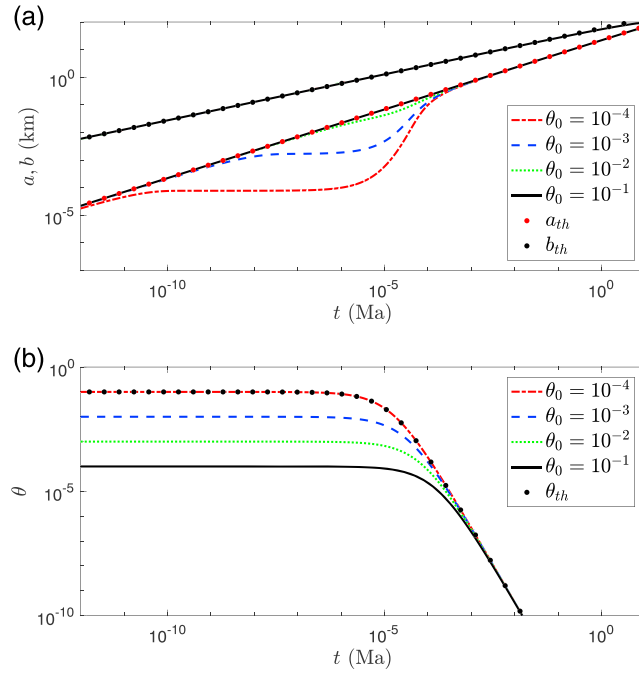


Figure 4. Representative numerical solutions (a) of the crustal thickness, a , and core radius, b , and (b) of the superheat, θ , in each case plotted for initial superheat $\theta_0 = 0.1$ (red dash-dotted line), 0.01 (blue dashed line), 0.001 (green dotted line), and 0.0001 (black solid line), and for $R = 150$ km and representative values as indicated in Table 1. Overlain are the asymptotic solutions in (a) for the crustal thickness from (39) and the inner core radius from (44) (black dots), and in (b) the asymptotic expression for the superheat from (41) (black dots) calculated for $\theta_0 = 0.1$.

$$\frac{\partial \theta}{\partial t} = -3 \frac{\kappa}{R} \frac{(R-a)^2}{[(R-a)^3 - b^3]} (1-a/R)^{1/3} \mathcal{F}_T \theta^{4/3}, \quad (37)$$

$$\frac{\partial b}{\partial t} = \frac{\kappa}{R} \left(\frac{R-a}{b} \right)^2 \mathcal{F}_S (1-a/R)^{1/3}, \quad (38)$$

where we have reintroduced the reduced temperature $\theta = (\bar{T} - T_m)/\Delta T$ of the liquid core.

The behavior of the full numerical solutions is shown in Figure 4. Growth of the crust is, at all times, driven by conductive cooling through the crust and limited by, variously, the release of latent heat at the interface, a convective heat flux from the interior, and the delamination of the viscous crust. At very early times, when the crustal thickness $a \ll R$, the primary balance is between conductive heat losses and latent heat release, and growth of the crust is well approximated by the classical model of Stefan growth

$$a = 2\lambda \sqrt{\kappa t}, \quad (39)$$

with $\lambda \simeq 1.06$ for $S = 0.2$. After the initial Stefan growth, a steady state balance is conceivable between conductive cooling and viscous delamination that would result in a constant crustal thickness. However, this occurs only when

$$\frac{\kappa}{a} = \frac{\kappa}{R} (1-a/R)^{1/3} \frac{\mathcal{F}_S}{2\gamma_e} \quad (40)$$

is satisfied which requires a value $\mathcal{F}_S/(2\gamma_e) \geq 4^{4/3}/3 \simeq 2.1$, whereas for the representative values above $\mathcal{F}_S/(2\gamma_e) \approx 0.41$. In contrast, given the strength of the initial convective thermal flux, $(\kappa/R)\mathcal{F}_T\theta^{4/3}$, it is likely that a balance exists between conductive cooling and convective heating from the interior at intermediate times (see Figure 4a). The balance leads to a pause in crustal thickening at relatively thin crustal thicknesses $a \simeq 2\lambda^2 SR/\mathcal{F}_T\theta_0^{4/3}$ at early times $t_1 \simeq (R^2/\kappa)(\lambda S/\mathcal{F}_T\theta_0^{4/3})^2$, similar to the pause in the crustal growth of magma chambers (Huppert & Worster, 1992). This balance between conductive cooling and convective heating leading to a pause in crustal thickening persists until the superheat of the planetesimal

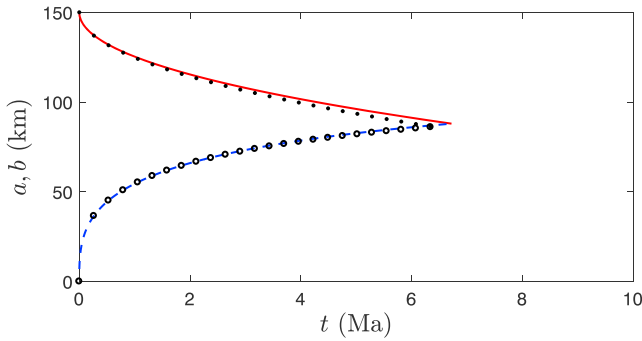


Figure 5. Reduced model (no superheat, $\theta = 0$) showing the growth of the crust, $a(t)$ (red solid line), and inner core, $b(t)$ (blue dashed line). Also shown for comparison are the asymptotic solutions for the thickness of the crust from equation (39) (solid dots) and the inner core radius from equation (44) (circles).

interior is exhausted. Since the crust is thin while the superheat is exhausted, $a \ll R$, we may write, to excellent approximation, that

$$\theta = \theta_0 \left[1 + \mathcal{F}_T \theta_0^{1/3} \frac{\kappa t}{R^2} \right]^{-3} = \theta_0 \left[1 + \left(\frac{Ra_f \theta_0}{Ra_c} \right)^{1/3} \frac{\kappa t}{R^2} \right]^{-3}, \quad (41)$$

where θ_0 is the initial superheat, and a comparison to the full numerical solution is shown in Figure 4b. This indicates that any superheat within the planetesimal interior will be rapidly exhausted by conduction through the iron crust. The timescale for the rapid decrease in superheat can be estimated as

$$t_2 \simeq \frac{R^2}{\kappa} \left(\frac{Ra_c}{Ra_f \theta_0} \right)^{1/3}. \quad (42)$$

For example, when the initial liquid interior temperature is $\bar{T} = T_m + 20$ K, and hence $\theta_0 = (\bar{T} - T_m)/(T_m - T_s) = 0.0125$, the time at which superheat begins to rapidly decay is approximately 31 years. For unmantled

planetesimals, superheat can therefore be expected to play a negligible role in the evolution of the planetesimal crust and growth of the solid core. Mantled cores, however, would not display this insensitivity to the initial superheat.

Perhaps more importantly, the rapid decay in superheat implies that the solid crust will be too thin to preserve any magnetic record from this epoch. As a result, any observed remnant magnetism is unlikely to be caused by a thermally driven dynamo but must instead rely on the buoyancy flux associated with delamination. Given the separation between thermal growth of the crust and viscous delamination, the leading-order feedback between the solid flux and the radial growth is the dependence of the gravitational acceleration on gravity, given by equation (28). The solid flux may therefore be well approximated by

$$F_s \simeq \frac{\kappa \Delta \rho}{R} \left(\frac{2\lambda^2}{\gamma_e} \right)^{2/3} \left(1 - \frac{2\lambda\sqrt{\kappa t}}{R} \right)^{1/3} \left(\frac{Ra_s}{7K_T} \right)^{1/3}, \quad (43)$$

with implications for driving the generation of a persistent magnetic field as discussed in the following section.

The relatively small estimates of the delamination flux, $\mathcal{F}_S \ll 1$, and the rapid decay of superheat for times $t \geq t_2$ imply a return to the balance between thermal conduction through the crust and the release of latent heat. Hence, the crustal growth is given, to good approximation at late times, by equation (39). Thus, for the nominal parameters considered here delamination is a minor contributor to the growth of the solid crust—but it nonetheless controls whether or not a dynamo occurs (see below).

The decoupling of crustal growth from delamination allows us to integrate equation (38) directly to find an expression for the core radius with time,

$$b = R \left(\frac{27\mathcal{F}_S}{260\lambda^2} \right)^{1/3} \left[1 - \left(1 - \frac{2\lambda\sqrt{\kappa t}}{R} \right)^{10/3} \left(1 + \frac{20\lambda\sqrt{\kappa t}}{3R} \right) \right]^{1/3}. \quad (44)$$

The solution to equations (36) and (38), neglecting superheat at all times, $\theta = 0$, is shown in Figure 5 and shows reasonable agreement between the simple Stefan growth model of the crust (equation (39)) and the full core growth model including the effects of crustal delamination (equation (44)).

In general, solidification of the asteroid is complete when the sum of the crustal thickness and core radii equal the planetesimal radius, $a + b = R$. In Figure 6 we show the numerically determined final thickness of the crust, a_∞ , and the time to solidify, t_∞ , by the solid blue curve and find that $a(t \rightarrow \infty) = a_\infty \simeq 62.1$ km, for $\mathcal{F}_S = 3.31$ and $R = 150$ km. The curves also show that two regimes are possible, depending principally on the size of the planetesimal. When the scaled solid flux $\mathcal{F}_S = \mathcal{F}_S(R) \ll 1$, roughly equivalent to $R \ll 100$ km, the growth of the crust and core are as described above. In contrast, when $\mathcal{F}_S \gg 1$ or $R \gg 1,000$ km, delamination

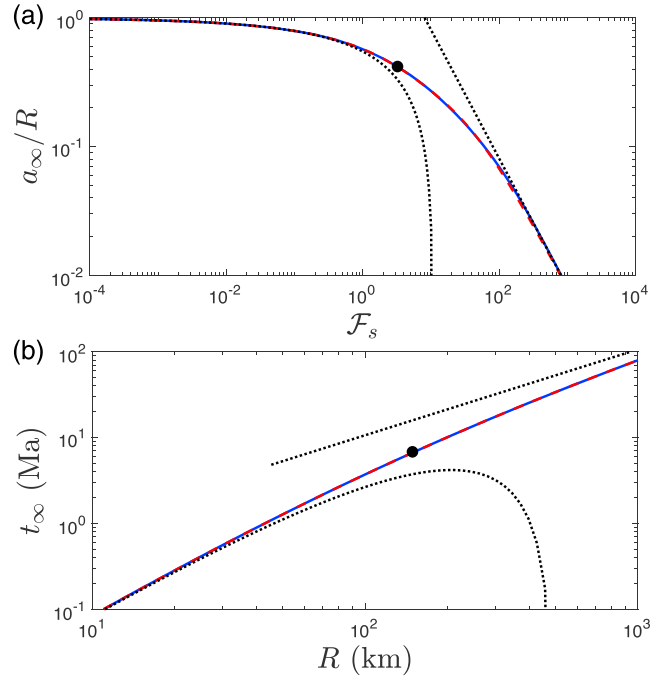


Figure 6. (a) The fractional final crustal thickness as a function of the scaled solidification flux (solid blue) along with approximate expressions for $\mathcal{F}_S \ll 1$ and $\mathcal{F}_S \gg 1$ (dotted black line, equation (45)) along with a composite expression (dashed red line, equation (46)). (b) The total time taken for solidification for representative parameter values and as a function of the asteroid radius, R , (solid blue line) is shown along with approximate expressions for $\mathcal{F}_S \ll 1$ and $\mathcal{F}_S \gg 1$ (dotted black line, (47)) along with a composite expression (dashed red line, equation (48)). The values for a planetesimal with radius $R = 150$ km are marked with a black dot and are $\mathcal{F}_S = 3.31$, $a_\infty = 62.1$ km, and $t_\infty = 6.7$ Ma.

may balance crustal growth leading to a constant crustal thickness. The two limits on crustal thickness are therefore

$$\frac{a_\infty}{R} = \begin{cases} 1 - (9\mathcal{F}_S/65)^{1/3} & \mathcal{F}_S \ll 1, \\ 2\gamma_e/\mathcal{F}_S & \mathcal{F}_S \gg 1, \end{cases} \quad (45)$$

as shown by the dotted black lines in Figure 6a. A composite expression, giving the final crustal thickness to within 0.1%, is

$$\frac{a_\infty}{R} = \frac{1 - (27\mathcal{F}_S/(260\lambda^2))^{1/3} + b_1\mathcal{F}_S^{2/3}}{1 + b_2\mathcal{F}_S^{1/3} + b_3\mathcal{F}_S^{2/3} + b_4\mathcal{F}_S + b_5\mathcal{F}_S^{4/3} + b_1\mathcal{F}_S^{5/3}/(2\gamma_e)}, \quad (46)$$

where $b_1 = 0.13$, $b_2 = 0.01$, $b_3 = 0.07$, $b_4 = 0.15$, and $b_5 = -0.06$, as shown by the dashed red curve in Figure 6a.

Similarly, the time to fully solidify a planetesimal may be written as a function of the radius and displays two regimes; either solidification time is determined by crustal growth ($\mathcal{F}_S \ll 1$ or equivalently $R \ll 100$ km) or by the growth of the inert inner core ($\mathcal{F}_S \gg 1$ or equivalently $R \gg 1,000$ km). The two limits on the solidification time are given by

$$\frac{t_\infty}{R^2/\kappa} = \begin{cases} \frac{1}{4\lambda^2} \left[1 - (27\mathcal{F}_S/(260\lambda^2))^{1/3} \right]^2 & \mathcal{F}_S \ll 1, \\ 1/(3\mathcal{F}_S) & \mathcal{F}_S \gg 1, \end{cases} \quad (47)$$

as shown by the dotted black lines in Figure 6b. A composite expression, giving the solidification time to within 0.1%, is

$$\frac{t_\infty}{R^2/\kappa} = \frac{[1 - (27\mathcal{F}_S/(260\lambda^2))^{1/3}]^2/(4\lambda^2) + c_1\mathcal{F}_S}{1 + c_2\mathcal{F}_S^{1/3} + c_3\mathcal{F}_S^{2/3} + c_4\mathcal{F}_S + c_5\mathcal{F}_S^{4/3} + c_6\mathcal{F}_S^{5/3} + 3c_1\mathcal{F}_S^2}, \quad (48)$$

where $c_1 = 0.04$, $c_2 = 0.001$, $c_3 = -0.02$, $c_4 = 0.20$, $c_5 = 0.05$, and $c_6 = 0.08$, as shown by the dashed red curve in Figure 6b. It is worth noting that the composite expressions, equations (46) and (48), are written using the nondimensional solid delamination flux, \mathcal{F}_S , and so are equally valid for different estimates of the physical parameters listed in Table 1. Finally, it is worth noting that for a planetesimal of radius $R = 150$ km (for which $\mathcal{F}_S = 3.31$ given the parameter values listed in Table 1), the final crustal thickness is $a_\infty = 62.1$ km which forms over a time $t_\infty = 6.7$ Ma as indicated by the black dots in Figure 6.

2.4. Dynamo Generation

Empirical scaling relationships can be used to estimate the expected properties of the magnetic field from the buoyancy flux predicted by the evolution model outlined in the previous section. Here we use relationships that have been derived from numerical simulations with Earth-like geometries, that is, a growing inner core that eventually occupies the entire core radius and no inward solidification. While there is currently some debate as to their efficacy, and indeed equivalent relationships have yet to be derived for top-down solidification, they currently provide the best means of assessing magnetic field properties so we choose to use modified versions of the equations presented in Bryson et al. (2015), based on those from Nimmo (2009) and Olson and Christensen (2006).

First, due to the large heat flux out of an unmantled body and the fast core cooling rate, we might expect that thermally driven convection of core liquid would be more likely on the IVA parent body than within mantled bodies (Nimmo, 2009). However, once solidification starts and the evolution of the core is governed by the balance between latent heat and cooling, the liquid quickly becomes isothermal at the liquidus temperature T_m (see section 2.3.1). Since the liquid at the base of the crust remains at this temperature, there is no driving thermal buoyancy flux driving convection, and so we can discount thermal convection as a possible long-lived dynamo-driving mechanism.

The solid flux (equation (28)) was used to calculate the properties of compositionally driven convection due to sinking delaminated material. From this parameter, a buoyancy flux can be calculated as

$$F_b = \frac{4}{3} \pi g (R - a) \frac{F_s}{\rho} = \frac{g_0 \kappa}{R} \frac{4\pi}{3} \mathcal{F}_S (1 - a/R)^{4/3}. \quad (49)$$

It is worth noting at this stage that the values of F_b in this study are significantly greater than those calculated for other studies on small bodies (Bryson et al., 2015; Elkins-Tanton et al., 2011; Nimmo, 2009; Weiss et al., 2010) reflecting the large heat flux out of an unmantled body and the large density contrast between the solid diapirs and core liquid. For example, using representative values (see Table 1), we find a maximum buoyancy flux at the surface ($a = 0$ km) to be $F_b = 1.4 \times 10^{-10}$ m²/s³. Field intensity is expected to scale with buoyancy flux (Olson & Christensen, 2006), so these large predicted F_b values are consistent with the field properties inferred from experimental studies of type IVA asteroids (Bryson et al., 2017). Other previously identified dynamo-driving mechanisms are unlikely to produce these large values of F_b , reinforcing delamination as a plausible dynamo-driving mechanism on the IVA parent body.

The buoyancy flux was then used to calculate the flux-based Rayleigh number,

$$Ra_Q = \frac{F_b}{d^2 \Omega^3} \frac{R}{a + b} = \frac{g_0 \kappa}{\Omega^3 R^3} \frac{4\pi}{3} \mathcal{F}_S \frac{(1 - a/R)^{4/3}}{(1 - a/R - b/R)^2 (a/R + b/R)}, \quad (50)$$

where $d = R - a - b$ is the distance over which the solid can sink and hence drive fluid motion, $\Omega = 2\pi/p$ is the rotation frequency of the parent body, and $p = 15, 120$ s is the rotation period (Hanus et al., 2013). This value is taken as that of the present-day period of the asteroid 16 Psyche, the largest metallic body in the asteroid belt.

From the flux-based Rayleigh number, the key properties of the magnetic field can be estimated. For example, the magnetic Reynolds number, which dictates whether convection will result in a magnetic field, is expressed as

$$\begin{aligned} R_m &= 0.85 \frac{\Omega d R}{\lambda_m} Ra_Q^{2/5}, \\ &= 0.85 \frac{\Omega R^2}{\lambda_m} \left(\frac{g_0 \kappa}{\Omega^3 R^3} \frac{4\pi}{3} \mathcal{F}_S \right)^{2/5} \frac{(1 - a/R - b/R)^{1/5} (1 - a/R)^{8/15}}{(a/R + b/R)^{2/5}}, \end{aligned} \quad (51)$$

where $\lambda_m = 1.2$ m²/s is the magnetic diffusivity (Weiss et al., 2010). For values of $R_m > 10$, magnetic fields have been predicted to result from convection on small bodies (Weiss et al., 2010), a regime applicable for

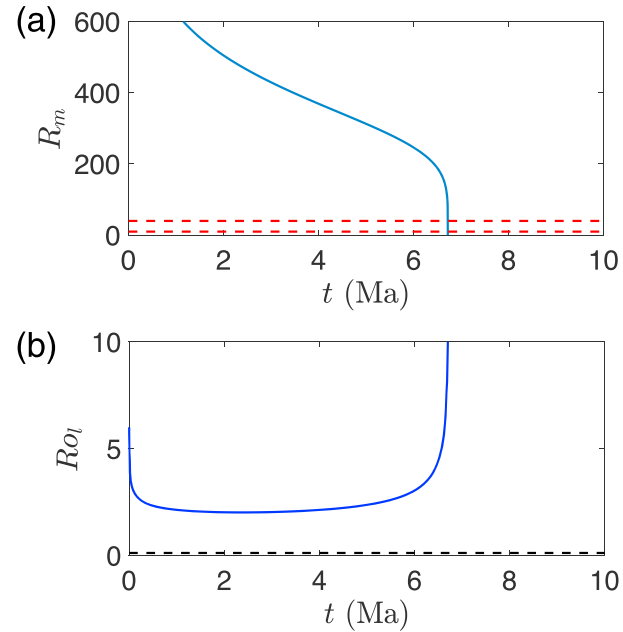


Figure 7. (a) The predicted magnetic Reynolds number across the period of solidification. The predicted critical value for small bodies ($R_m = 10$; Weiss et al., 2010) and Earth-sized bodies ($R_m = 40$; Olson & Christensen, 2006) are included. (b) The local magnetic Rossby number, Ro_l (solid blue line), is plotted along with the boundary between dipolar and multipolar dynamos ($Ro_l > 0.12$, black dashed line).

the entire period of solidification predicted by our model. Magnetic fields have been predicted for values of $R_m > 40$ on Earth-sized bodies (Olson & Christensen, 2006), which is predicted for nearly the complete period of solidification (see Figure 7a).

The local Rossby number, which dictates the polarity of the field, can be expressed as

$$\begin{aligned}
 Ro_l &= 0.58 \frac{Ra_Q^{1/2}}{E_k^{1/3}} \left(\frac{Pr}{Pr_m} \right)^{1/5}, \\
 &= 0.58 \left(\frac{g\kappa}{\Omega^3 R^3} \frac{4\pi}{3} F_s \right)^{1/2} \left(\frac{\Omega R^2}{\nu} \right)^{1/3} \left(\frac{\lambda_m}{\kappa} \right)^{1/5} \frac{(1 - a/R)^{2/3}}{(1 - a/R - b/R)^{1/3} (a/R + b/R)^{1/2}},
 \end{aligned} \tag{52}$$

where $E_k = \nu/\Omega d^2$ is the Ekman number, $Pr = \nu/\kappa$ is the Prandtl number, $Pr_m = \nu/\lambda_m$ is the magnetic Prandtl number, and $\nu = \mu_f/\rho = 10^{-6}$ m²/s is the nominal kinematic viscosity of the liquid (Weiss et al., 2010). This empirical relationship was derived from numerous numerical models of dynamo generation, which tended to display magnetic reversals during the multipolar regime and during the dipolar regime near the dipolar-multipolar transition. We therefore use the local Rossby number as a proxy for likelihood of generating a directionally unstable magnetic field and predict directional instability in the magnetic field across the entire period of solidification. For $Ro_l > 0.12$ a multipolar field is predicted, which, again, is the case for the entire period of solidification (Figure 7b).

These results suggest that the buoyancy flux created by delamination events is therefore sufficient to produce a strong, long-lasting, and multipolar magnetic field consistent with paleomagnetic measurements of IVA asteroids (Bryson et al., 2017).

3. The Effects of Composition

A potential complication to this relatively straightforward approach is the distribution of incompatible elements within a solidifying planetesimal, a possibility which has been raised previously by Scheinberg et al. (2016). In general, the presence of any number of light, incompatible elements may alter both the density of the liquid interior and the local freezing temperature through the phase diagram. In large planetary systems, the rejection of light impurities on solidification of the planetary core from the bottom up is a significant driver of convection and hence of the generation of planetary magnetic fields. In contrast, the rejection of

light impurities during top-down solidification produces a stratified compositional layer, whose principal effect is to produce a stagnant, partially solid (or mushy) crust, the dynamics of which we explore below.

The model developed in the preceding sections can be adapted to incorporate the distribution of sulfur, a relatively abundant light element within most planetesimal cores. As with the previous study of Scheinberg et al. (2016), we use the simplified iron-sulfur phase diagram of Ehlers (1972), approximating the depression of the melting temperature along the liquidus as

$$T_L(C) = T_m - mC, \quad (53)$$

for moderate sulfur concentration, C , where we take $T_m = 1810$ K as before and the slope of the liquidus as $m = 18$ K/wt%. The rejection of a light impurity, such as sulfur, leads to constitutional supercooling at the solid-liquid interface, $R - a$, and the formation of a partially solid crust, often referred to as a mushy layer (Worster, 1997). In this region the constitutional supercooling is relieved by the growth of a porous solid, of solid fraction ϕ , bathed in a sulfur (or light element)-rich liquid of liquid fraction $1 - \phi$. Due to the high surface area of contact within the porous matrix, the composition of this interstitial fluid lies along the liquidus to excellent approximation. Since the composition is then enriched in sulfur and, to good approximation, the fluid density is more strongly a function of composition than temperature, this produces a (compositionally) stably stratified fluid within the porous mushy layer.

An important consequence is that during solidification, the sulfur rejected on solidification remains trapped within a stably stratified mushy layer save for a negligibly small diffusive flux into the liquid core. The impact of the inclusion of sulfur on the much larger-scale cooling of the planetesimal and the putative generation of a magnetic field is then chiefly to alter the rheological properties of the solidifying iron crust by further weakening the base of the convecting, now partially solid, boundary layer. The thermal argument described in the preceding sections therefore remains largely the same, though with a correction accounting for the weakened rheology of the mushy crust. The solidifying crust contains a porous, and therefore rheologically weak, lower boundary layer the rheology and thickness of which is now determined both by the thermal structure within the crust and the solid fraction within the mushy base. This weak lower boundary layer periodically delaminates to form diapirs which descend through the liquid outer core to form an inner core of radius b . A potential complication of compositional variations is that the mushy boundary layer now also contains compositionally enriched fluid. If that fluid remains within the mushy layer during delamination and subsequent foundering to form the core, the bulk composition of the liquid remains unchanged throughout the planetesimals evolution. If instead the interstitial fluid is expelled, which seems likely, it will drive a secular variation in the bulk composition of the liquid, with implications for the evolution of the mushy layer porosity and rheology.

In this latter scenario, compaction of the mushy layer is most likely to occur either during the delamination of the boundary layer or in the subsequent formation of the core. If compaction predominantly occurs during delamination, the expelled interstitial liquid would be released at the top of the liquid core, potentially stratifying the liquid, with implications for the evolving rheology of the crust, but with an otherwise negligible role in driving the magnetic field due to the lack of compositional convection. In contrast, if compaction primarily occurs when mushy diapirs of crustal material coalesce to form the core (Scheinberg et al., 2016), the release of compositionally buoyant interstitial fluid at the base of the liquid core could enhance, or drive, fluid motion resulting in a stronger magnetic field as well as a general increase in the bulk composition of the liquid. The details of these processes are sufficiently complex that we leave them for later study but instead proceed with a parameterized model which captures the rheological effect of the mushy crust on magnetic field generation through solid delamination and the secular evolution of the bulk composition through compaction.

To model simply the formation of a partially molten, or mushy, base of the crust, we assume that the thermal structure is much the same as that determined in the absence of light impurities. In practice, the thermal structure is slightly altered as the release of latent heat occurs throughout the mushy zone rather than simply at a planar solid-liquid interface. However, we leave such a detailed study to future work.

Within the mush layer, the stratification of light, incompatible elements leads to a stagnant interstitial fluid. Conservation of composition may therefore be expressed as

$$(1 - \phi) \frac{\partial C}{\partial t} = (C - C_s) \frac{\partial \phi}{\partial t}, \quad (54)$$

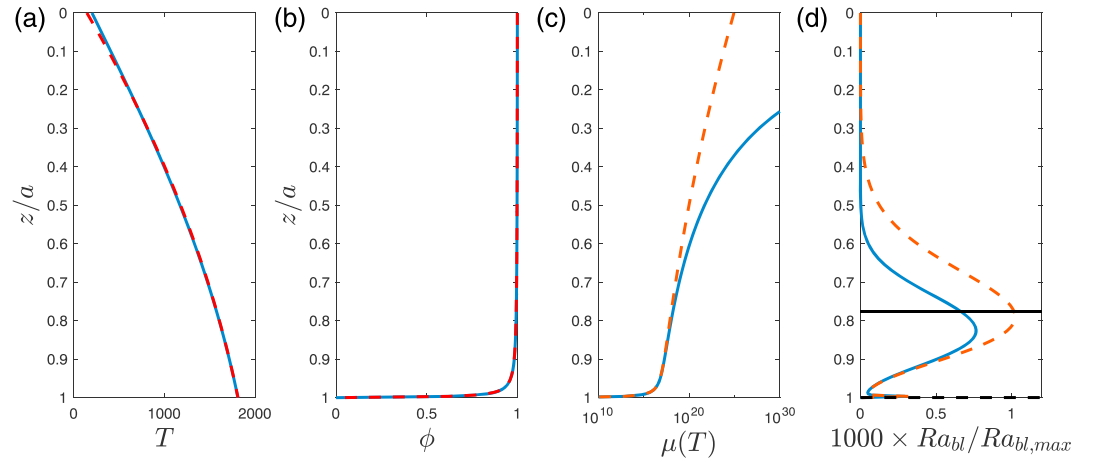


Figure 8. Profiles through the crust of (a) the temperature T , (b) the solid fraction ϕ , and (c) the viscosity $\mu(T, \phi)$ for $\bar{C} = 0.1$ with the profiles (solid blue line) and approximate solutions (dashed red line) shown. (d) The boundary layer Rayleigh number, which exhibits two maxima at $z/a = 0.9997$ (dashed line) and $z/a = 0.78$ (solid line) corresponding to modes of delamination controlled by the solid fraction variation and thermal structure, respectively.

where $\phi(z, t)$ is the bulk solid fraction and $C_s \simeq 0$ is the concentration of light impurity within the solid. Within the stagnant mushy layer, the interstitial composition C is closely tied to the temperature through phase equilibrium so that we can integrate equation (54) to show that the composition within the mushy layer is that of the bulk liquid, $(1 - \phi)C = \bar{C}$. Hence, the liquid fraction may be written

$$1 - \phi = \frac{\bar{C}}{C}, \quad (55)$$

where $\bar{C}(t)$ is the bulk concentration of soluble impurities in the liquid core. Again, within the mushy layer temperature and composition are constrained to lie along the liquidus, and we may approximate the thermal field as

$$\begin{aligned} T &\simeq T_L(\bar{C}) - 2\lambda^2 S(T_L(\bar{C}) - T_s)(1 - z/a) [1 + \lambda(1 - z/a)], \\ &= T_m - m\bar{C} - 2\lambda^2 S(\Delta T - m\bar{C})(1 - z/a) [1 + \lambda(1 - z/a)], \end{aligned} \quad (56)$$

so that near the mush-liquid interface the liquid fraction is

$$1 - \phi = \frac{\bar{C}}{C} = \frac{m\bar{C}}{m\bar{C} + 2\lambda^2 S(\Delta T - m\bar{C})(1 - z/a) [1 + \lambda(1 - z/a)]}. \quad (57)$$

We use a simple extension of the Arrhenius model for the viscosity of the solid crust (equation (17)) to account for the variations in solid fraction,

$$\mu_s = \mu_{s0} \exp \left[\frac{E_\mu}{R_g} \left(\frac{1}{T} - \frac{1}{T_m} \right) - E_\phi(1 - \phi) \right], \quad (58)$$

$$\simeq \mu_{s0} \exp \left[\frac{E_\mu(T_m - T)}{R_g T_m^2} - \frac{E_\phi m\bar{C}}{T_m - T} \right], \quad (59)$$

which provides a good approximation to the viscosity near the base of the crust where $T \simeq T_m - m\bar{C}$ and incorporates the expected reduction in viscosity with increasing melt fraction (Mei et al., 2002). Equivalently, using equations (56) and (57), we can write

$$\mu_s \simeq \mu_{s0} \exp \left[\gamma f(C, z/a) - \frac{E_\phi C}{f(C, z/a)} \right], \quad (60)$$

where $\gamma \simeq 8.0$ is defined as in equation (19) and

$$C = \frac{m\bar{C}}{2\lambda^2 S \Delta T} \quad \text{and} \quad f(C, z/a) = C + (1 - 2\lambda^2 S C)(1 - z/a) [1 + \lambda(1 - z/a)]. \quad (61)$$

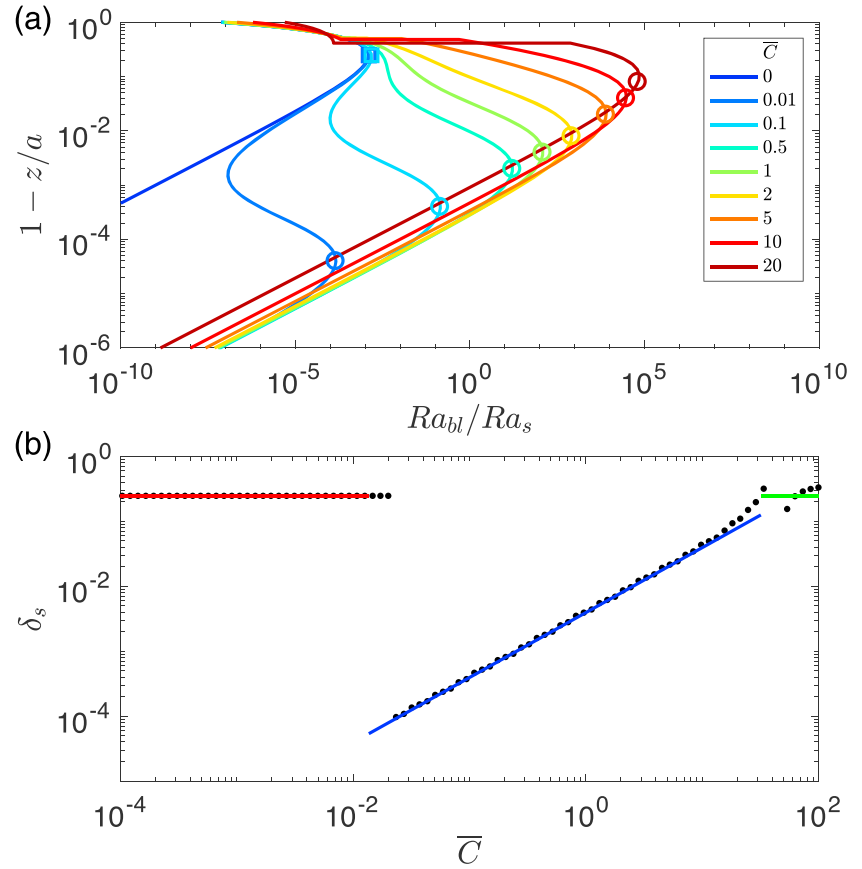


Figure 9. (a) Profiles of the Ra_{bl} for a sequence of bulk liquid compositions, $\bar{C} = 0, 0.01, 0.1, 0.5, 1, 2, 5, 10, 20$ wt% ($C = 0.00014, 0.0014, 0.0069, 0.014, 0.028, 0.069, 0.14, 0.49$), along with the approximate points of maximal Ra_{bl} , (δ_s, Ra_{bl}) , for the thermal mode (squares) and for the mushy mode of delamination (circles). (b) The numerically determined boundary layer depth corresponding to the maximal Ra_{bl} (points) is plotted with the thermal limit (red line), porosity limit (blue line), and eutectic limit (green line) as given in (64).

Note that, for the parameters in this study, the composition scale $2\lambda^2 S\Delta T/m \simeq 71.4$ wt%. Again, we construct a boundary Rayleigh number, as in equation (20), now with contributions from the thermal structure and profile of solid fraction in the crust

$$Ra_{bl}(z) = \frac{g\Delta\rho\phi(z)(a-z)^3}{\kappa\mu(T(z), \phi(z))}. \quad (62)$$

A representative example is shown in Figure 8, which shows the profiles in temperature, solid fraction, viscosity, and Ra_{bl} for the case $C = 0.002$, ($\bar{C} = 0.14$ wt%). The profiles demonstrate the effect that a small boundary of high-porosity (high melt fraction) crust has on the viscosity structure which gives rise to two modes of convection: a mushy mode of delamination governed by the rheologically weak, but narrow, mushy (low solid fraction) base of the crust, and the other thermal delamination mode determined by the broader, warm region at the base of the crust (replicating the structure shown in Figure 3 when $\phi \simeq 1$). This is reflected in the structure of $Ra_{bl}(z)$, as plotted in Figure 8d, which shows a maximum in Ra_{bl} associated with the narrow boundary layer in porosity (at $z/a = 0.9997$) and the broad thermal boundary layer (at $z/a = 0.83$). An expansion of Ra_{bl} , plotted with a logarithmic scale that highlights these two competing modes of convection for varying \bar{C} is shown in Figure 9a. The relative magnitudes of these thermal and porosity boundary layers may be determined as a function of the nondimensional bulk liquid composition, \bar{C} . We can find approximate expressions for the maxima in Ra_{bl} , and hence the depth of the delaminating boundary layer, by finding the roots of

$$\left. \frac{\partial Ra_{bl}}{\partial z} \right|_{z=z_c} = 0 = \frac{C}{f^2} \frac{(1-z/a)^3}{e^f} \frac{f}{z} - \frac{3(1-C/f)(1-z/a)^2}{e^f} - \frac{f(1-C/f)(1-z/a)^3}{z e^f}, \quad (63)$$

which provides an estimate of the boundary layer thickness as

$$\delta_{s,\phi}/a = \gamma_{e,\phi}^{-1} = \begin{cases} \delta_{s,\phi1} = \left(-1 + \sqrt{1 + 24\lambda/\gamma}\right)/4\lambda & 0 < C < C^*, \\ \delta_{s,\phi2} = 3C/(E_\phi - 6) & C^* < C < C_E, \\ \delta_{s,\phi3} = \left(-1 + \sqrt{1 + 24\lambda/\gamma}\right)/4\lambda & C > C_E. \end{cases} \quad (64)$$

The thickness of the delaminating solid boundary layer, $\delta_{s,\phi}$, is determined by the location of the maximum in the boundary Rayleigh number, Ra_{bl} , which switches discontinuously between thermal and porosity modes. We find that for small bulk compositions, $C < C^*$, the solid boundary layer thickness is determined by the thermal boundary layer and the effects of porosity weakening are negligible, while for larger bulk compositions, $C > C^*$, the effects of porosity weakening become dominant and delamination is dominated by the low-porosity boundary layer. The critical concentration at which the dominant mode switches is $C^* \simeq 3.4 \times 10^{-4}$ (for the parameters used in this study $C^* = 0.014$ wt%) and may be found by solving for the composition where $Ra_{bl}(\delta_{s,\phi1}, C^*) = Ra_{bl}(\delta_{s,\phi2}, C^*)$.

The physical consequence of this behavior is that there is a discontinuous switch from the thermal mode of convection to the porosity-dominated mode of convection as the bulk liquid concentration increases and hence a discontinuous jump in the convective flux. It is also worth noting that the mushy lower boundary of the crust that is significantly weakened by the presence of melt is typically very narrow, and hence the boundary layer thickness which delaminates is significantly smaller. For example, for a bulk composition $\bar{C} = 0.01$ wt%, $C = 1.4 \times 10^{-4}$ and $\delta_s = 0.247a$, which, for $a \simeq 10$ km implies $\delta_s = 2.47$ km, while for $\bar{C} = 0.1$ wt%, $C = 1.4 \times 10^{-3}$ and $\delta_s = 2 \times 10^{-4}a$ or $\delta_s = 2$ m for an equivalent crustal thickness. It is also worth noting that for temperatures below the eutectic, $T < T_e$, the crust is solid, $\phi = 1$, which occurs at a position

$$z_E/a = 1 - \frac{-1 + \sqrt{1 - 4\lambda(C - C_E)/(1 - C)}}{2\lambda}, \quad C_E = \frac{T_m - T_e}{2\lambda^2 S \Delta T}, \quad (65)$$

as reflected in the profiles of $Ra_{bl}(z)$ depicted in Figure 9. Here $C_E \simeq 0.8$ ($C_E = 32$ wt%) for the parameters used in this study.

We may now straightforwardly extend the previous model to include the presence of light impurities. The depth of the unstable boundary layer, $\delta_{s,\phi}$, is now given by equation (64) which delaminates over a timescale

$$t_{s,\phi}^* = \frac{\gamma_e \delta_{s,\phi}^{*2}}{2\lambda^2 \kappa} \simeq \frac{\gamma_e}{2\lambda^2 \kappa} \left(\frac{14\lambda^2 K_T}{\gamma_{e,\phi}} \frac{\mu_{s0,e} \kappa}{\Delta \rho g(r)} \right)^{2/3}, \quad (66)$$

where for simplicity we take a discontinuous end point viscosity

$$\mu_{s0,e} = \begin{cases} \mu_{s0} & 0 < C < C^*, \\ \mu_{s0} e^{\gamma C} & C^* < C < C_E, \\ \mu_{s0} e^{\gamma C_E} & C > C_E. \end{cases} \quad (67)$$

This end point viscosity increases with increasing concentration following the depression of the freezing point as determined by the phase diagram (equation (53)) evaluated at the mush-liquid interface where $C = \bar{C}$. It is worth recalling that the full temperature- and liquid fraction-dependent viscosity is given by equation (60).

The solid flux is now

$$F_{s,\phi} = \bar{\phi} \Delta \rho \frac{\delta_{s,\phi}^*}{t_{s,\phi}^*} \simeq \bar{\phi} \frac{\kappa \Delta \rho}{R} \left(\frac{2\lambda^2}{\gamma_{e,\phi}} \right)^{2/3} (1 - a/R)^{1/3} \left(\frac{Ra_s}{7C} \frac{\mu_{s0}}{\mu_{s0,e}} \right)^{1/3}, \quad (68)$$

where we have calculated the averaged solid fraction over the porous boundary layer,

$$\bar{\phi} = \frac{1}{\delta_{s,\phi}} \int_{a-\delta_{s,\phi}}^a \phi(z) dz \simeq 1 - \frac{\gamma C}{1 - C} \ln \left(1 + \frac{1 - C}{\gamma C} \right), \quad (69)$$

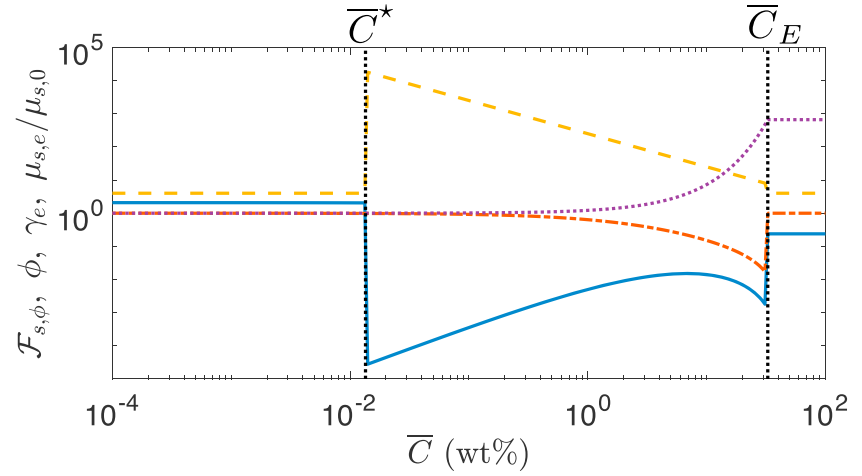


Figure 10. The magnitude of the solid delamination flux, $\mathcal{F}_{s,\phi}$ (blue solid line); the average solid fraction, $\bar{\phi}$ (red dash-dotted line); the inverse boundary layer thickness, γ_e (orange dashed line); and the effective viscosity, $\mu_{s,e}/\mu_{s,0}$ (purple dotted line) are plotted as a function of the bulk composition \bar{C} , where, for the values used in this study, $\bar{C}^* = 0.14$ wt% and $\bar{C}_E = 32$ wt%.

using equation (57). A representative example of $\bar{C} = 1$ wt%, for which $C = 0.014$ we find that the mean solid fraction $\bar{\phi} \simeq 0.74$ and that a boundary layer of characteristic thickness $\delta_{s,\phi}^* \simeq 80$ m delaminates on a timescale of $t_s^* \simeq 375$ kyr.

Hence, including the effect of light impurities, the conservation of energy at the delaminating boundary may be written as (cf. equation (31))

$$\rho L \bar{\phi} \frac{\partial a}{\partial t} = k \left. \frac{\partial T}{\partial z} \right|_{a^-} - c_p \left(\frac{T_L(\bar{C}) - T_c}{2} \right) \mathcal{F}_{s,\phi}, \quad (70)$$

where as before T_c represents the temperature at the top of the delaminating layer and now $T_L(\bar{C})$ is the temperature at the mush-liquid interface. We may also rearrange to find the equivalent energy conservation equation (analogous to equation (36)) incorporating the nonzero melt fraction at the base of the crust,

$$\bar{\phi} S \frac{\partial a}{\partial t} = 2\lambda^2 S \frac{K}{a} - 2\lambda^2 S \frac{K}{R} (1 - a/R)^{1/3} \frac{\mathcal{F}_{s,\phi}}{2\gamma_{e,\phi}}, \quad (71)$$

where now the magnitude of the solid delamination flux is

$$\mathcal{F}_{s,\phi} = \bar{\phi} \frac{\Delta\rho}{\rho} \left(\frac{2\lambda^2}{\gamma_{e,\phi}} \right)^{2/3} \left(\frac{Ra_s}{7K_T} \frac{\mu_{s0}}{\mu_{s0,e}} \right)^{1/3}, \quad (72)$$

where Ra_s and K_T are as defined previously. This equation makes it clear that there are three modes of delamination. For very small concentrations ($C < C^*$) $\bar{\phi} \simeq 1$; the viscosity, and hence the boundary layer depth as characterized by $\gamma_{e,\phi}$, is determined by the thermal structure, and the delamination flux approaches the pure case ($\bar{C} = 0$ wt% as discussed in section 2). For larger compositions ($\bar{C} > C^*$) the much weaker, thin, high-porosity mushy zone at the base of the crust dominates delamination. While delamination events are more frequent, they also carry significantly less mass so that the mass flux, $\mathcal{F}_{s,\phi}$, is significantly reduced. Finally, for eutectic compositions ($\bar{C} = C_E$) the crust is again solid, $\bar{\phi} = 1$, and the delamination flux becomes larger, comparable to the pure value, modified slightly as the viscosity is larger at the eutectic temperature, $T_L(C_E)$. These trends in the magnitude of the solid delamination flux, $\mathcal{F}_{s,\phi}$, the average solid fraction, $\bar{\phi}$, the inverse boundary layer length, γ_e , and the effective end point viscosity, $\mu_{s,e}/\mu_{s,0}$, are shown in Figure 10 as a function of the bulk liquid composition, \bar{C} .

The evolution of the concentration of light impurity in the liquid interior, $\bar{C}(t)$, is difficult to constrain without a simplifying model of the growth and deformation of the mushy crust. The interstitial fluid may remain within the mushy layer during delamination and subsequent foundering, with the implication that the bulk liquid composition remains unchanged throughout planetesimal solidification, $\bar{C} \simeq \text{constant}$. In this case, while the formation of a mushy layer alters the rheological properties of the crust, and hence the solid flux,

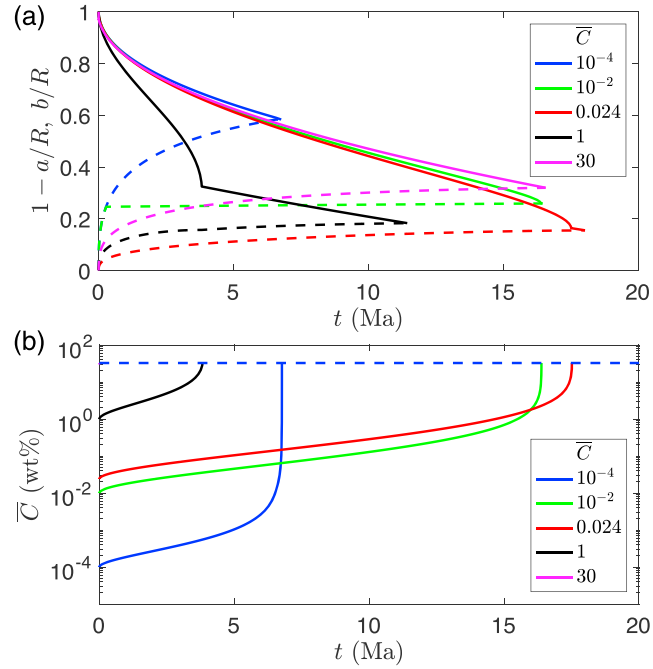


Figure 11. (a) The evolution of the crustal thickness, $a(t)$ (solid line), and core radius, $b(t)$ (dashed line) for initial bulk liquid compositions $\bar{C}(0) = 10^{-4}$ wt% (blue), 10^{-2} wt% (green), 0.024 wt% (red), 1 wt% (black), and 30 wt% (pink). (b) The evolution of the bulk liquid concentration from the initial value, $\bar{C}(0)$, to the eutectic value, \bar{C}_E (indicated by the dashed horizontal lines). Note that $\bar{C} \rightarrow \bar{C}_E$ extremely rapidly, within ~ 400 years, for $\bar{C}(0) = 30$ wt%.

these properties remain constant through the planetesimal evolution such that the dynamics are broadly comparable to the case of pure solidification, $\bar{C} = 0$ wt%. Conversely, when the interstitial fluid is expelled from the mushy layer either on delamination or through compaction during solid core growth, the bulk composition of the liquid evolves. Here we assume (for illustrative purposes) that all the interstitial fluid is expelled from the mushy layer throughout the deformation process and that this compositionally enriched fluid is rapidly mixed throughout the fluid core. If the mushy diapirs compact, expelling their buoyant interstitial fluid as they form the core, then we may model the growth of the compacted core by

$$\rho_s 4\pi b^2 \frac{\partial b}{\partial t} = 4\pi(R - a)^2 F_s, \quad (73)$$

or, written in a manner analogous to equation (38), by

$$\frac{\partial b}{\partial t} = \frac{\kappa}{R} \left(\frac{R - a}{b} \right)^2 (1 - a/R)^{1/3} \mathcal{F}_{S,\phi}. \quad (74)$$

The light, compositionally enriched material released on compaction readily mixes with the bulk liquid driving an evolution of the bulk concentration, $\bar{C}(t)$. If all the light incompatible elements are efficiently rejected on compaction, and rapidly stirred by delamination events, then the bulk concentration may be simply related to its initial value by

$$\frac{4}{3}\pi [(R - a)^3 - b^3] \bar{C}(t) = \frac{4}{3}\pi R^3 \bar{C}(0), \quad (\bar{C} < C_E) \quad (75)$$

or equivalently as

$$\bar{C} = \begin{cases} \bar{C}(0) / [(R - a)^3 - b^3] & (R - a)^3 - b^3 > \bar{C}(0)/C_E \\ C_E & (R - a)^3 - b^3 < \bar{C}(0)/C_E \end{cases} \quad (76)$$

Here we note that when the liquid concentration $\bar{C} \rightarrow C_E$ the solid formed is again pure (and of the eutectic concentration), and the dynamics of delamination are described by those discussed in section 2. The results

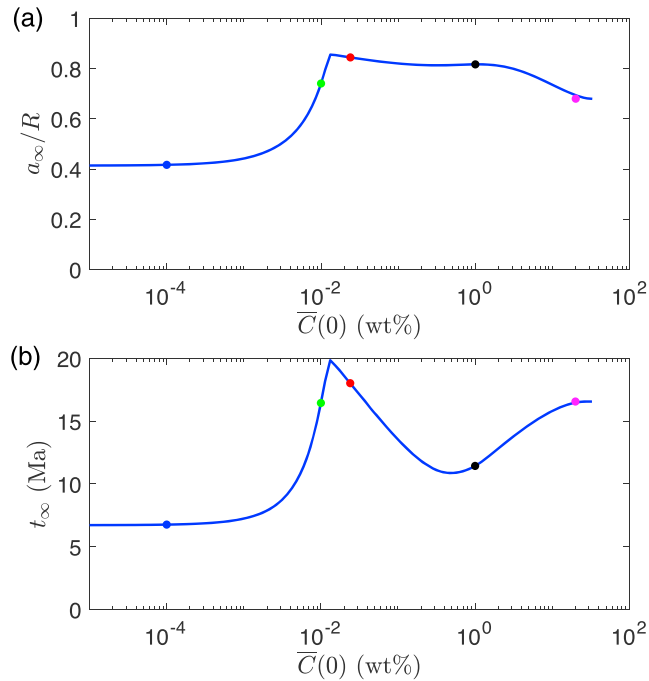


Figure 12. (a) The final crustal thickness as a function of the initial bulk concentration, $\bar{C}(0)$, and (b) the total time for solidification. All calculations are for radius $R = 150$ km. The colored dots indicate the exemplar solutions for $\bar{C}(0) = 10^{-4}, 10^{-2}, 0.024, 1, 30$.

of the compacting core model are shown in Figures 11 and 12. Figure 11a shows the fractional thickness of the crust (solid) and core (dashed) over time for five different initial values of the bulk concentration, $\bar{C}(0)$, and Figure 11b shows the corresponding trajectories in fluid composition, $\bar{C}(t)$. It is worth noting that for finite initial concentration ($\bar{C} \neq 0$ wt%) all models finish their evolution with a eutectic composition liquid, though those cases with higher initial composition ($\bar{C}(0)$) spend proportionally longer with $\bar{C} = C_E$. This is perhaps most clearly seen at intermediate concentrations (e.g., $\bar{C} = 1$ wt% in Figure 11a) where the initial crustal growth, $a(t)$, is determined by the thermal, and then mushy, modes of delamination followed by a dramatic reduction in the growth rate as $\bar{C} = C_E$ signifying the onset of the eutectic mode of delamination. It is also worth noting that in the limit $\bar{C}(0) \rightarrow 0$ wt% the model for pure iron discussed in section 2 is recovered exactly.

This change in overall dynamics with initial concentration, $\bar{C}(0)$, is also reflected in the final crustal thickness and the total time for solidification plotted in Figure 12. Again, for very low bulk impurity concentrations, $\bar{C}(0) \lesssim 10^{-3}$ wt%, the pure iron evolution is recovered exactly. As the initial impurity concentration increases, the time for final solidification initially increases (as expected), and the final thickness of the crust relative to the core also increases. Both effects arise because for larger concentrations, where greater time is spent with $C^* < C < C_E$, the result is a weaker time-averaged delamination flux dominated by the mushy mode of delamination, and hence a longer solidification time and smaller final core radius (thicker crust). This trend is reversed for large enough initial bulk concentrations, since the period during which the bulk concentration is at the eutectic, $\bar{C} = C_E$ (see, e.g., $\bar{C} = 0.024$ wt%, red curve in Figure 11), is extended resulting in a larger time-averaged delamination flux. In an extreme case, the compositional and crustal evolution may at all times be dominated by eutectic mode of delamination ($\bar{C} = 30$ wt% in Figure 11).

The addition of impurities thus affects the detailed dynamics of the delamination flux and the timescales of solidification but plays a relatively minor role in the evolution of the buoyancy flux available for driving a magnetic field. Following the previous analysis, we find that for all initial bulk concentrations considered the magnetic Reynolds number is always sufficiently large to suggest that strong magnetic fields are produced by the delamination flux as shown in Figure 13a. Similarly, the values of the local Rossby number suggest that these fields are multipolar, consistent with the observations of the IVA meteorites.

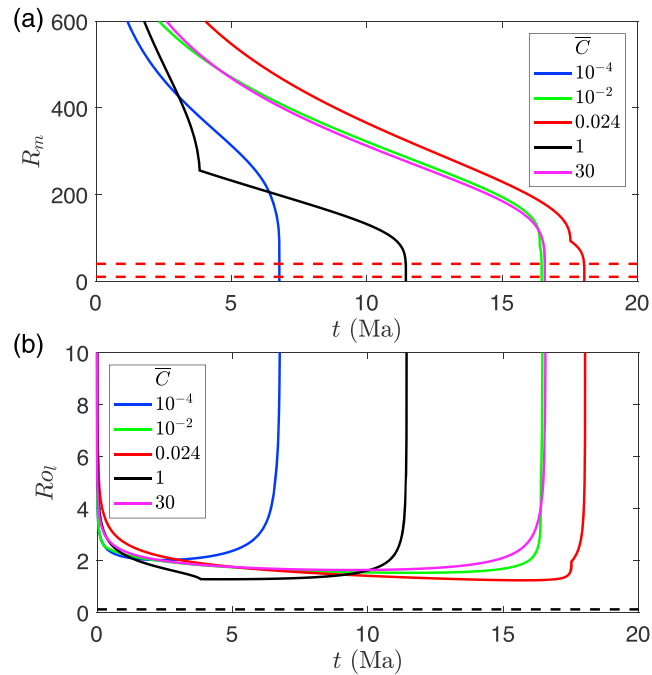


Figure 13. (a) The magnetic Reynolds number is plotted along with the boundaries for magnetic field generation on small ($R_m > 10$) and large ($R_m > 40$) bodies and (b) the local Rossby number is plotted along with the boundary between dipolar and multipolar dynamos ($R_{ol} > 0.12$, black dashed line), in both figures for initial concentrations $\bar{C}(0) = 10^{-4}$, 10^{-2} , 0.024, 1, 30. These results suggest that for all concentrations considered, a strong, multipolar magnetic field should be prevalent during the course of planetesimal solidification.

4. Discussion and Conclusions

We have presented simplified models of the rapid solidification of unmantled asteroid cores that crystallized from the surface inward. Paleomagnetic measurements of the IVA meteorites indicate that intense, directionally varying fields were generated on such bodies. These observations present a significant challenge as top-down solidification cannot generate a dynamo through the same mechanism as the cores of much larger bodies which solidify from the bottom up. Here we have suggested that delamination of a weak, warm boundary layer at the base of an inwardly crystallizing metallic crust at the surface of metallic asteroids creates a buoyancy flux that is sufficient to generate a dynamo with intense, directionally varying magnetic fields and to record those fields in the colder solid crust above.

This scenario most closely resembles the modeling of Scheinberg et al. (2016) who posited the detachment of dendrites and rate of growth and melting of iron crystals in the liquid core as the most potent driver of dynamo activity and magnetic fields in unmantled cores. In that study, while the possibility of delamination was raised, the detailed numerical modeling instead considered cumulate formation of unattached dendrites within the liquid core, which rapidly descended to form the inner core. Here, we instead focus on macroscopic delamination, such that the viscosity structure of the crust is an important factor that crucially determines the rates of convective mixing through a buoyancy flux driven by delamination. We consider two main drivers of the buoyancy flux with the potential for dynamo generation: thermal convection driven by the difference between the freezing temperature of iron and the mean temperature of the liquid core, and the delamination flux of the weak base of the crust. Conservation of energy at the evolving boundary results in a relatively simple, modified Stefan model for solidification, thermal convection, and delamination. The results of this model suggest that thermal buoyancy rapidly (within $\sim 1,000$ years) becomes negligible. Although the cooling rates of the IVA iron meteorites are fast compared to those of other iron meteorite groups (Goldstein et al., 2009), they still cooled on the order of thousands to hundreds of degrees per million years and so could not have recorded this transient field. Instead, we find that viscous delamination of a metallic crust is sufficient to drive magnetic field over much of the ~ 10 -Ma lifetime of a Psyche-sized body (e.g., of radius $R = 150$ km) and so is far more likely to be the origin of the remanent magnetization carried by the IVA iron meteorites. Moreover, we predict that this field was intense and multipolar, matching

the properties of the magnetic field inferred from paleomagnetic measurements of the IVA iron meteorites (Bryson et al., 2017), and this model can also explain the inward crystallization trends observed in this meteorite group. We therefore suggest that the major driver of dynamo activity in unmantled cores could have been the delamination of inwardly crystallizing metallic crusts.

The presence of light, insoluble impurities, such as sulfur, results in a mushy (sometimes referred to as dendritic) zone at the base of the crust where light impurities rejected during solidification stagnate. The net effect of such a mushy, partially solid zone is to further reduce the effective viscosity at the base of the crust. We suggest that this leads to two distinct forms of delamination: a broader thermal mode active at very low compositions that is commensurate with the thermal structure at the base of the crust and a much narrower and weaker mushy mode active at higher concentrations that is associated with the region of lower solid fraction. While these two modes alter the details of delamination, their effect is relatively minor on either the magnitude of magnetic field generation or the duration of solidification. Their primary impact may be instead on the compositional stratification of the solidified core. If solute is ejected from the compacting diapirs that form the solid core of the planetesimal, this results in a gradual buildup of concentration in the liquid as the planetesimal solidifies, driving the bulk liquid concentration to the eutectic in all cases. This suggests a third, eutectic mode of delamination, again controlled by the thermal structure, now of a solid eutectic-composition crust. It also suggests that most planetesimals should have nearly pure crust and core, with a eutectic composition annulus in the interior (the width of which depends on the initial bulk liquid composition and the radius). It is this compositional structure, along with the commensurate predictions of the thermal structure and magnetic field intensities, that provide the strongest testable hypotheses and which may be addressed by the upcoming Psyche mission.

Acknowledgments

J. A. N. is partly funded by the University Research Fellowship from the Royal Society. F. N. acknowledges support from the NASA-EW program. All figure data are available from the Cambridge data repository (<https://doi.org/10.17863/CAM.37924>).

References

- Asphaug, E., Agnor, C. B., & Williams, Q. (2006). Hit-and-run planetary collisions. *Nature*, *439*, 155–160.
- Bryson, J. F. J., Nichols, C. I. O., Herrero-Albillos, J., Kronast, F., Kasama, T., Alimadadi, H., et al. (2015). Long-lived magnetism from solidification-driven convection on the Pallasite parent body. *Nature*, *517*, 472–475. <https://doi.org/10.1038/nature14114>
- Bryson, J. F. J., Weiss, B. P., Harrison, R. J., Herrero-Albillos, J., & Kronast, F. (2017). Paleomagnetic evidence for dynamo activity driven by inward crystallisation of a metallic asteroid. *Earth and Planetary Science Letters*, *472*, 152–163.
- Carporzen, L., Weiss, B. P., Elkins-Tanton, L. T., Shuster, D. L., Ebel, D., & Gattacceca, J. (2011). Magnetic evidence for a partially differentiated carbonaceous chondrite parent body. *Proceedings of the National Academy of Sciences*, *108*, 6386–6389. <https://doi.org/10.1073/pnas.1017165108>
- Chabot, N. L. (2004). Sulfur contents of the parental metallic cores of magmatic iron meteorites. *Geochimica et Cosmochimica Acta*, *68*, 3607–3618.
- Christensen, U. R. (2015). Iron snow dynamo models for Ganymede. *Icarus*, *247*, 248–259.
- Davaille, A., & Jaupart, C. (1993). Transient high-Rayleigh-number thermal convection with large viscosity variations. *Journal of Fluid Mechanics*, *253*, 141–166.
- Dwyer, C. A., Stevenson, D. J., & Nimmo, F. (2011). A long-lived lunar dynamo driven by continuous mechanical stirring. *Nature*, *479*, 212–214.
- Ehlers, E. G. (1972). *The interpretation of geological phase diagrams*. San Francisco, CA: W. H. Freeman.
- Elkins-Tanton, L. T., Weiss, B. P., & Zuber, M. T. (2011). Chondrites as samples of differentiated planetesimals. *Earth and Planetary Science Letters*, *305*, 1–10.
- Frost, H. J., & Ashby, M. F. (1982). *Deformation-mechanism maps, the plasticity and creep of metals and ceramics*. Oxford: Pergamon Press.
- Fu, R. R., Weiss, B. P., Shuster, D. L., Gattacceca, J., Grove, T. L., Suavet, C., et al. (2012). An ancient core dynamo in asteroid Vesta. *Science*, *338*, 238–241.
- Ghosh, A., & McSween, H. Y. Jr (1998). A thermal model for the differentiation of asteroid 4 Vesta, based on radiogenic heating. *Icarus*, *134*, 187–206.
- Goldstein, J. I., Scott, E. R. D., & Chabot, N. L. (2009). Iron meteorites: Crystallization, thermal history, parent bodies and origin. *Geochemistry*, *69*(4), 293–325.
- Haack, H., Rasmussen, K. L., & Warren, P. H. (1990). Effects of regolith/megaregolith insulation on the cooling histories of differentiated asteroids. *Journal of Geophysical Research*, *95*(B4), 5111–5124.
- Haack, H., & Scott, E. R. D. (1992). Asteroid core crystallization by inward dendritic growth. *Journal of Geophysical Research*, *97*(E9), 14,727–14,734.
- Hanus, J., Marchis, F., & Durech, J. (2013). Sizes of main-belt asteroids by combining shape models and Keck adaptive optics observations. *Icarus*, *226*, 1045–1057.
- Hauck, S. A. II, Aurnou, J. M., & Dombard, A. J. (2006). Sulfur's impact on core evolution and magnetic field generation on Ganymede. *Journal of Geophysical Research*, *111*, E09008. <https://doi.org/10.1029/2005JE002557>
- Hevey, P. J., & Sanders, I. S. (2006). A model for planetesimal meltdown by ^{26}Al and its implications for meteorite parent bodies. *Meteoritics and Planetary Science*, *41*(1), 95–106.
- Howard, L. N. (1964). Convection at high Rayleigh number. In H. Görtler & P. Sorger (Eds.), *Applied Mechanics, Proceedings of the 11th International Congress of Applied Mechanics* (pp. 1109–1115). Berlin, Germany: Springer-Verlag.
- Huppert, H. E., & Worster, M. G. (1992). Vigorous motions in magma chambers and lava lakes. In D. Yuen (Ed.), *Chaotic Processes in Geological Sciences* (pp. 141–174). New York: Springer-Verlag.
- Kleine, T., Touboul, M., Bourdon, B., Nimmo, F., Mezger, K., Palme, H., et al. (2009). Hf-W chronology of the accretion and early evolution of asteroids and terrestrial planets. *Geochimica et Cosmochimica Acta*, *73*, 5150–5188.

- Laneuville, M., Wieczorek, M. A., Breuer, D., Aubert, J., Morard, G., & Rückriemen, T. (2014). A long-lived lunar dynamo powered by core crystallization. *Earth and Planetary Science Letters*, *401*, 251–260.
- Le Bars, M., Wieczorek, M. A., Karatekin, Ö., Cébron, D., & Laneuville, M. (2011). An impact-driven dynamo for the early Moon. *Nature*, *479*, 215–218.
- Mei, S., Bai, W., Hiraga, T., & Kohlstedt, D. L. (2002). Influence of melt on the creep behavior of olivine-basalt aggregates under hydrous conditions. *Earth and Planetary Science Letters*, *201*, 491–507.
- Molnar, P., Houseman, G. A., & Conrad, C. P. (1998). Rayleigh-Taylor instability and convective thinning of mechanically thickened lithosphere: Effects of non-linear viscosity decreasing exponentially with depth and of horizontal shortening of the layer. *Geophysical Journal International*, *133*, 568–584.
- Neumann, W., Breuer, D., & Spohn, T. (2014). Differentiation of Vesta: Implications for a shallow magma ocean. *Geophysical Research Letters*, *39*(5), 267–280.
- Nimmo, F. (2009). Energetics of asteroid dynamos and the role of compositional convection. *Geophysical Research Letters*, *36*, L10201. <https://doi.org/10.1029/2009GL037997>
- Olson, P., & Christensen, U. R. (2006). Dipole moment scaling for convection-driven planetary dynamos. *Earth and Planetary Science Letters*, *250*, 561–571.
- Opeil, C. P., Consolmagno, G. J., & Britt, D. T. (2010). The thermal conductivity of meteorites: New measurements and analysis. *Icarus*, *208*(1), 449–454.
- Riley, D. S., Smith, F. T., & Poots, G. (1974). The inward solidification of spheres and circular cylinders. *International Journal of Heat and Mass Transfer*, *17*, 1507–1516.
- Rückriemen, T., Breuer, D., & Spohn, T. (2014). Key characteristics of the Fe-snow regime in Ganymede's core. *Lunar and Planetary Science Conference*, *45*, 2454.
- Scheinberg, A., Elkins-Tanton, L. T., Schubert, G., & Bercovici, D. (2016). Core solidification and dynamo evolution in a mantle-stripped planetesimal. *Journal of Geophysical Research: Planets*, *121*, 2–20. <https://doi.org/10.1002/2015JE004843>
- Scheinberg, A., Soderlund, K. M., & Schubert, G. (2015). Magnetic field generation in the lunar core: The role of inner core growth. *Icarus*, *254*, 62–71.
- Sterenborg, M. G., & Crowley, J. W. (2013). Thermal evolution of early solar system planetesimals and the possibility of sustained dynamos. *Physics of the Earth and Planetary Interiors*, *214*, 53–73.
- Tarduno, J. A., Cottrell, R. D., Nimmo, F., Hopkins, J., Voronov, J., Erickson, A., et al. (2012). Evidence for a dynamo in the main group pallasite parent body. *Science*, *338*, 939–942.
- Tkalcic, B. J., Golabek, G. J., & Brenker, F. E. (2013). Solid-state plastic deformation in the dynamic interior of a differentiated asteroid. *Nature Geoscience*, *6*, 93–97.
- Vilim, R., Stanley, S., & Hauck, S. A. II (2010). Iron snow zones as a mechanism for generating Mercury's weak observed magnetic field. *Journal of Geophysical Research*, *115*, E11003. <https://doi.org/10.1029/2009JE003528>
- Weiss, B. P., Berdahl, J. S., Elkins-Tanton, L., Stanley, S., Lima, E. A., & Carporzen, L. (2008). Magnetism on the angrite parent body and the early differentiation of planetesimals. *Science*, *322*, 713–716. <https://doi.org/10.1126/science.1162459>
- Weiss, B. P., & Elkins-Tanton, L. T. (2013). Differentiated planetesimals and the parent bodies of chondrites. *Annual Review of Earth and Planetary Sciences*, *41*(1), 529–560. <https://doi.org/10.1146/annurev-earth-040610-133520>
- Weiss, B. P., Gattacceca, J., Stanley, S., Rochette, P., & Christensen, U. R. (2010). Paleomagnetic records of meteorites and early planetesimal differentiation. *Space Science Reviews*, *152*, 341–390.
- Wettlaufer, J. S. (2001). The Stefan problem: Polar exploration and the mathematics of moving boundaries. In C. Hammerl, R. Lenhard, R. Steinacker, & P. Steinhauser (Eds.), *Die Zentralanstalt für Meteorologie und Geodynamik, 1851-2001, 150 Jahre Meteorologie und Geophysik in Österreich* (pp. 420–435). Graz, Austria: Styria Verlag.
- Williams, Q. (2009). Bottom-up versus top-down solidification of the cores of small solar system bodies: Constraints on paradoxical cores. *Earth and Planetary Science Letters*, *284*, 564–569.
- Worster, M. G. (1997). Convection in mushy layers. *Annual Reviews of Fluids Mechanics*, *29*, 91–122.
- Yang, J., & Goldstein, J. I. (2006). Metallographic cooling rates of the IIIAB iron meteorites. *Geochimica et Cosmochimica Acta*, *70*, 3197–3215.
- Yang, J., Goldstein, J. I., & Scott, E. R. D. (2007). Iron meteorite evidence for early formation and catastrophic disruption of protoplanets. *Nature*, *446*, 888–891.
- Yang, J., Goldstein, J. I., & Scott, E. R. D. (2008). Metallographic cooling rates and origin of IVA iron meteorites. *Geochimica et Cosmochimica Acta*, *72*, 3043–3061.
- Yang, J., Goldstein, J. I., & Scott, E. R. D. (2010). Main-group pallasites: Thermal history, relationship to IIIAB irons, and origin. *Geochimica et Cosmochimica Acta*, *74*, 4471–4492.